International Journal of Plasticity 136 (2021) 102887

Contents lists available at ScienceDirect

International Journal of Plasticity

journal homepage: http://www.elsevier.com/locate/ijplas

Comparative assessment of backstress models using high-energy X-ray diffraction microscopy experiments and crystal plasticity finite element simulations

Ritwik Bandyopadhyay [a], Sven E. Gustafson [a,1], Kartik Kapoor [a,1], Diwakar Naragani [a], Darren C. Pagan [b], Michael D. Sangid [a,*]

[a] School of Aeronautics and Astronautics, Purdue University, West Lafayette, IN, USA
[b] Cornell High Energy Synchrotron Source, Ithaca, NY, USA

ARTICLE INFO

Keywords:
Cyclic plasticity
Back stress
Armstrong-Frederick
Geometrically necessary dislocation (GND)
Backstress saturation

ABSTRACT

Crystal plasticity (CP) models have been evolving since their inception. Advanced experimental characterization methods have contributed significantly to assess the performance and subsequent improvement of many empirical relations in CP, which were directly adopted from classical plasticity theories of solids at the macro-scale. In this research, high energy X-ray diffraction microscopy (HEDM) has been used to track the stress-state of individual grains within a polycrystalline aggregate of a Nickel-base superalloy subjected to cyclic loading. Using path-dependent, mesoscopic stress-states from the HEDM experiment, the performance of two kinematic hardening models, in the context of CP, has been assessed. One of the models is an empirical Armstrong-Frederick equation, and the other is a geometrically necessary dislocation (GND)-based phenomenological model. The results suggest that the GND-based model is capable of capturing the cyclic crystal plasticity response. The present validation efforts are expected to take CP models one step closer towards their implementation in modern engineering workflow.

1. Introduction

An appropriate crystal plasticity model is expected to capture the salient features that are associated with the elasto-plastic deformation of a metallic material subjected to monotonic loading, and ideally, more complex loading paths. Especially, in the context of cyclic loading, the key features, at the macroscopic length-scale, include but are not limited to the cyclic hardening and softening, the Bauschinger effect, ratcheting, mean stress relaxation, and elastic shakedown (Suresh, 1998). Kinematic hardening models are often incorporated within the framework of crystal plasticity to capture the Bauschinger effect under strain-controlled cyclic loading. The present paper is focused on the comparative assessment of two kinematic hardening models, one being empirical and another phenomenological, in the context of crystal plasticity theory.

Historically, crystal plasticity theory was developed to incorporate the mechanisms of plastic deformation, precisely dislocation glide (Taylor, 1934), within the paradigm of continuum description of plastic deformation in metals. In 1971, using an internal-variable theory, Rice established a generalized framework for crystal plasticity constitutive relations for finite elasto-plastic

* Corresponding author.
E-mail address: msangid@purdue.edu (M.D. Sangid).
[1] These authors contributed equally to the manuscript.

https://doi.org/10.1016/j.ijplas.2020.102887
Received 8 April 2020; Received in revised form 8 September 2020; Accepted 24 September 2020
Available online 26 October 2020

deformation of metals (Rice, 1971). This work was a continuation of the earlier progress made by Bishop and Hill (1951), Hill (1967), and Rice (1970). One of the key outcomes from Rice's 1971 paper is that if the shearing rate ($\dot{\gamma}^i$) on the i^{th} slip system is only governed by a thermodynamic conjugate shear stress, π^i, corresponding to the same slip system, a flow potential can be derived and the normality structure follows. In the absence of residual stress, the thermodynamic conjugate shear stress on the i^{th} slip system, i.e., π^i, is related to the resolved shear stress (τ^i) on the same slip system as

$$\pi^i = \tau^i \lambda^i - \chi^i\left(\widehat{\mathbf{F}}, T, \gamma\right) \tag{1}$$

Here, $\widehat{\mathbf{F}}$ is the thermoelastic deformation gradient; λ^i is the stretch ratio along the slip direction of the i^{th} slip system; γ represents the current slipped-state of the material; $\chi^i(\widehat{\mathbf{F}}, T, \gamma)$ is the change in the free energy $\varphi(\widehat{\mathbf{F}}, T, \gamma)$ per unit shear rearrangement, when both temperature, T, and thermoelastic deformation gradient, $\widehat{\mathbf{F}}$, are held constant, i.e.,

$$\chi^i = \frac{\partial \varphi\left(\widehat{\mathbf{F}}, T, \gamma\right)}{\partial \gamma^i} \tag{2}$$

Under the assumption that the thermoelastic properties of the material are independent of the slip events, Rice decomposed $\varphi(\widehat{\mathbf{F}}, T, \gamma)$ as

$$\varphi\left(\widehat{\mathbf{F}}, T, \gamma\right) = \varphi^*\left(\widehat{\mathbf{F}}, T\right) + \varphi^{**}(T, \gamma) \tag{3}$$

Thus, Eq. (2) reduces to

$$\chi^i = \frac{\partial \varphi^{**}(T, \gamma)}{\partial \gamma^i} \tag{4}$$

Further, Rice set $\varphi^*(\widehat{\mathbf{F}}, T)$ to zero at the stress-free state of the material and offered an interpretation of $\varphi^{**}(T, \gamma)$ as the residual free-energy density of the material, if the crystal were taken from its current state to a stress-free intermediate configuration without changing γ or the current slipped-state (Rice, 1971). McDowell and Moosbrugger referred to χ^i as the slip system backstress (McDowell and Moosbrugger, 1990). Further, based on Rice's interpretation of $\varphi^{**}(T, \gamma)$, McDowell and Moosbrugger commented that χ^i is associated with the stored energy due to slip (McDowell and Moosbrugger, 1990). Thus, the concept of backstress, earlier introduced as an internal-variable in classical plasticity theory to model kinematic hardening, was invoked in the context of crystal plasticity theory. With the transitioning from classical to crystal plasticity domain, the immediate task was to set up appropriate evolution equations for slip system backstress.

The Armstrong-Frederick (AF) model (Armstrong and Frederick, 1966) is perhaps the most popular kinematic hardening description in the classical plasticity literature, initially developed for multiaxial loading, where the evolution of χ^i is described as

$$\dot{\chi}^i = A\dot{\gamma}^i - A_D \chi^i |\dot{\gamma}^i| \tag{5}$$

Here, the constants A and A_D are associated with direct hardening and dynamic recovery, respectively. In 1991, the AF model was first applied to crystal plasticity by Méric et al. (1991) and Méric and Cailletaud (1991). After that, several researchers directly adopted Eq. (5) in their crystal plasticity framework (Bennett and McDowell, 2003; Castelluccio and McDowell, 2014, 2015; Goh et al, 2001, 2003, 2006; Harder, 1999; Hasija et al., 2003; Horstemeyer et al., 1999; Li et al., 2014; Mayeur et al., 2008; Mayeur and McDowell, 2007; Miller and McDowell, 1996; Prasannavenkatesan and McDowell, 2010; Smith et al., 2018; Tu et al., 2019; Venkataramani et al, 2006, 2008; Xie et al., 2004; Zhang et al, 2007, 2010). Based on the mathematical construct of Eq. (5), other kinematic hardening models have also been proposed, such as the Chaboche model (Chaboche, 1989a, 1989b, 1991; Chaboche et al., 1979) and the Ohno-Wang model (Ohno and Wang, 1993a), in the classical plasticity literature. The Chaboche model is a multi-dimensional representation of the AF model, where $\dot{\chi}^i$ is written as a linear summation of $\dot{\chi}^i_k$, i.e.,

$$\dot{\chi}^i = \sum_{k=1}^{N_B} \dot{\chi}^i_k \tag{6}$$

Here, each $\dot{\chi}^i_k$ follows an AF description, as given by Eq. (5), and N_B defines the dimension of the multi-dimensional representation. Clearly, the AF model involves two material constants (A and A_D), whereas the number of model parameters in the Chaboche model is $2N_B$ enabling the yield locus to be represented as multiple surfaces. On the other hand, Ohno and Wang (Ohno and Wang, 1993a, 1993b) slightly modified the dynamic recovery term in Eq. (5) and proposed the evolution of backstress as

$$\dot{\chi}^i = A\dot{\gamma}^i - A_D \left(\frac{|\chi^i|}{A/A_D}\right)^M \chi^i |\dot{\gamma}^i| \tag{7}$$

Here, M is an additional model parameter that controls the rate of dynamic recovery. The Ohno-Wang model involves three parameters (A, A_D and M), which is significantly lower than the Chaboche model. Some researchers have directly adopted Eq. (7) in their

description of kinematic hardening within a crystal plasticity framework (Cruzado et al, 2017, 2018). Although the models described in Eqs. (5)–(7) have their unique position in classical plasticity, direct adoption of these in crystal plasticity is of concern because of multiple reasons. First, these models (Eqs. (5)–(7)) are empirical and were meant for usage at the macroscopic length-scale to capture the Bauschinger effect and cyclic ratcheting. At the macro-scale, the Bauschinger effect and cyclic ratcheting are responses for cyclic deformation of metals, due to crystallographic slip and dislocation mechanisms operating at lower length-scales. Therefore, kinematic hardening models, in the context of crystal plasticity, are not only expected to capture the emerging behaviors at the macroscopic length-scale, but also the underlying mechanisms at a lower length-scale, especially for the realistic mechanical analysis of the material at the microstructural length-scale. Whether the models in Eqs. (5)–(7) can meet the latter requirement has not been rigorously verified in the literature. Second, when empirical models with a mathematically involved description of kinematic hardening at the macroscopic level are directly adopted at the slip system level, it is challenging to calibrate the associated (model) parameters experimentally. Indirect calibration or ad hoc fitting of these parameters eventually leads to uncertainty in the subsequent analysis. Such uncertainty, as well as a lack of validation and verification at the microstructural length-scale, have impeded the implementation of the crystal plasticity models in the modern engineering workflows (Shade et al., 2019).

Meanwhile, extensive experimental research has been conducted to understand the origin and underlying mechanisms of the Bauschinger effect at the microscopic length-scale. It was observed, particularly in FCC materials, that dislocations form wall structures during cyclic loading (Abel and Muir, 1972; Holt, 1970; Kuhlmann-Wilsdorf and Laird, 1977; Kuhlmann-Wilsdorf and Van Der Merwe, 1982; Laufer and Roberts, 1964; Mughrabi, 1983; Sleeswyk et al., 1978; Woods, 1973). In 1983, Mughrabi modeled such a structure within a crystal as a composite material, where dislocation walls represent a hard region with high dislocation density, and the region separating these walls is a relatively soft region of lower dislocation density (Mughrabi, 1983). Mughrabi showed that the dislocations in the interface of these two regions contribute to maintain compatibility during deformation and give rise to long-range internal stresses even in the absence of dislocation pile-ups. It was evident in Mughrabi's work that such long-range internal stresses at the microscopic level could potentially explain the Bauschinger effect at the macroscopic length-scale. Based on Ashby's interpretations of geometrically necessary dislocations (GNDs) (Ashby, 1970), Mughrabi's interfacial dislocations are equivalent to the concepts of GNDs. Thus, the notion that the GNDs could be used to model backstress, and thereby the Bauschinger effect, was incubated. Eventually, in 2018, inspired by the mathematical construct of Taylor-type (Taylor, 1934) slip system hardening, Kapoor et al. (2018) related χ^i to the GND density on the same slip system (ρ^i_{GND}) as

$$\chi^i = K\mu b^i \sqrt{\rho^i_{GND}} \tag{8}$$

Here, K is a scaling constant,[2] μ is the isotropic shear modulus of the material, and b^i is the Burgers vector corresponding to the i^{th} slip system. Thus, the GND-based backstress model, proposed by Kapoor et al., connected the mathematical description of kinematic hardening, in the context of crystal plasticity, to the underlying mechanisms at the microscopic level. It is also well-known that GNDs contribute significantly to the fraction of the energy stored by dislocation structures and substructures during plastic deformation (Zheng et al., 2019), albeit this may not be the case for low energy dislocation configurations that form under cyclic loading exhibiting zero net Burgers vector (Kuhlmann-Wilsdorf, 1989; Neumann, 1986). Therefore, given Eqs. (3) and (4), the model proposed by Kapoor et al. is also in close agreement with the thermodynamic origin of backstress in a pure continuum mechanics framework of crystal plasticity constitutive relations. Moreover, in the context of micropolar single crystal plasticity theory, researchers have demonstrated that backstress is a function of lattice torsion-curvature gradients (Forest, 2008; Mayeur et al., 2011; Mayeur and McDowell, 2013, 2014, 2015), which further supports the model proposed by Kapoor et al. (2018). In the literature, other researchers also connected the mathematical description of backstress to the underlying mechanisms of its origin before the work by Kapoor et al. Noteworthy contributions were made by Geers and co-workers (Bayley et al., 2006; Evers et al., 2004a, 2004b; Geers et al., 2007; Sauzay, 2008; Shenoy et al., 2008; Kim et al., 2012; Wollmershauser et al., 2012; Zecevic and Knezevic, 2015; Muhammad et al., 2017; Castelluccio and McDowell, 2017; Bhattacharyya et al., 2019; Eghtesad and Knezevic, 2019; Chen et al., 2019; El-Naaman et al., 2019 and Farooq et al., 2020). The work by Kapoor et al. stands unique because the initial GND density distribution can be characterized in a material using multiple techniques, such as electron backscatter diffraction, and thus, Eq. (8) enables one to initialize backstress at each point within a microstructure in the crystal plasticity analysis.

It is relatively easy to validate kinematic hardening models in classical plasticity using the macroscopic cyclic stress-strain response of the materials. In crystal plasticity, in addition to the macroscopic validation, one needs to ensure that the model can faithfully capture the response of the material at a relatively lower length-scale (Sangid et al., 2014). The first aspect, i.e., whether the kinematic hardening models in crystal plasticity can capture the macroscopic response, was addressed previously by other researchers (Hennessey et al., 2017; Schäfer et al., 2019). However, the second aspect, i.e., whether the same models can reasonably capture the response of the material at a relatively lower length-scale, has not been substantiated. One of the reasons behind a dearth of literature for such validation is the lack of appropriate experimental techniques capable of characterizing stress states within the microstructure of a polycrystalline aggregate. Recently, advances in high energy X-ray diffraction microscopy (HEDM) techniques have enabled

[2] Later, it will be evident in Eq. (17) that the computation of the GND density, i.e., ρ^i_{GND}, within the CPFE simulation framework requires evaluation of the derivatives, specifically Curl($\mathbf{F^P}$). Therefore, the resulting GND density is inherently dependent on the mesh size. The constant $K$is introduced to scale the term $\mu b^i \sqrt{\rho^i_{GND}}$to result in realistic backstress values at the length-scale of the finite element mesh. Thus, numerical value of $K$is inherently dependent on the mesh size and has to be figured out when the mesh size is chosen.

researchers to track the grain averaged stress within a polycrystalline aggregate as a function of macroscopic loading (Bernier et al., 2011; Margulies et al., 2002; Oddershede et al., 2010). Thus, new opportunities have emerged to validate the form for the constitutive equations in crystal plasticity theory using HEDM experiments.

In the present work, we assess the performance of two backstress models, in the context of crystal plasticity, by comparing the simulated response of the material to the response captured by HEDM experiments. One of the backstress models is the empirical AF-type (Armstrong and Frederick, 1966), and the other is a phenomenological GND-based description proposed by Kapoor et al. (2018). Other researchers have pointed out the limitations of the AF model and advocated other models, such as Ohno-Wang and Chaboche models (Cruzado et al., 2017; Hennessey et al., 2017; Schäfer et al., 2019). As described previously, the Chaboche model involves numerous parameters (see Eq. (6)), in which each additional parameter increases the uncertainty in the analysis. In terms of the number of parameters, both the Ohno-Wang and AF models offer similar advantages. However, none of the parameters associated with these two models can be currently measured directly from experimental data, which must be overcome via model calibration. With this, the Ohno-Wang model would perhaps be a better candidate than the AF model because of its more accurate (empirical) description of the kinematic hardening. However, we choose the AF model because of its mathematical simplicity and, consequently, popularity in the vast body of crystal plasticity literature within the class of empirical models. On the other hand, we select the GND-based model (Eq. (8)) as our second choice because it is physics-based and involves only one unknown parameter (K). With this, the scientific novelty of this work lies in the close coupling between in-situ HEDM experiments and crystal plasticity modeling, specifically comparing grain-level responses from crystal plasticity simulations to the same obtained from HEDM experiments under cyclic loading. The same type of analysis, used in this paper, could be employed to assess the reliability of other forms of constitutive backstress models.

The paper is structured as follows. In Section 2, the material chosen for the present work and the HEDM experimental method are described. In Section 3, the crystal plasticity finite element (CPFE) simulation framework is established. Results and accompanying discussions are presented in Section 4. Additional insights and remarks are offered in Section 5. Finally, conclusions are drawn in Section 6.

2. Materials and methods

2.1. Materials

The material chosen for the present work is 718Plus, an additively manufactured Nickel-base superalloy. ATI 718Plus® (Allegheny Technologies Incorporated, 2013) powder, referred to as 718Plus throughout this paper, is used and processed via selective laser melting using an EOS M280 laser powder-bed machine at Honeywell Aerospace. The build parameters are optimized via process modeling (Peralta et al., 2016) to result in minimal porosity (Gong et al., 2016). The optimized parameter values are 300 W laser power, 0.09 mm hatch spacing, 1.65 m/s laser speed, and stripe width of 5 mm. Following the build, the material is subjected to a suite of heat treatments to produce an optimal microstructure and preferred strength characteristics (Gong et al., 2016). A stress relief heat treatment is carried out at $1010^{\circ}C$ for 1.5 h with a flue gas quench followed by a hot isostatic pressure cycle at $1163^{\circ}C$ and 103 MPa for 4 h. Subsequently, the material is solution heat-treated at $1010^{\circ}C$ for 2 h with a flue gas quench and aged at $788^{\circ}C$ for 8 h followed by a ramp down at $39^{\circ}C$/h to reach $704^{\circ}C$ temperature. At $704^{\circ}C$, the material is held for 8 h then cooled in a furnace. After heat treatment, a tensile specimen, having 1500 μm gauge length and 1000 $\mu m \times 1000$ μm cross-sectional area at the gauge section (see

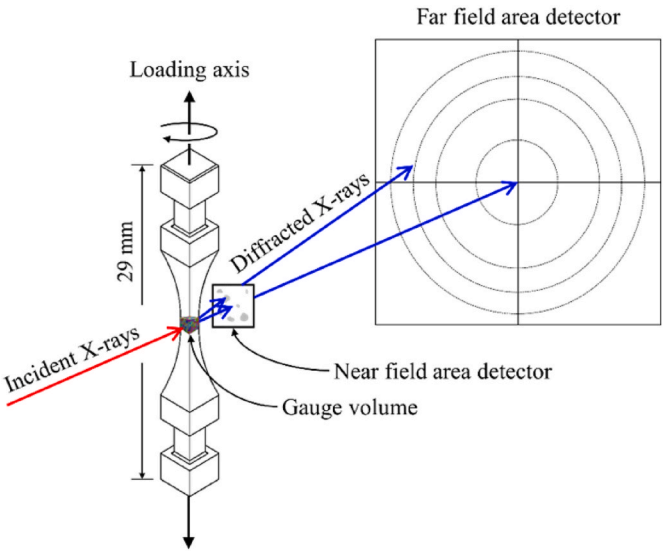

Fig. 1. Schematic of the high-energy X-ray diffraction microscopy setup.

Fig. 1), is machined for HEDM experiments.

2.2. High-energy X-ray diffraction microscopy

Multiple modalities of HEDM techniques are used to reconstruct the grain averaged orientations and full elastic strain tensors, and the 3D morphology of each grain within the illuminated volume of the material (see Fig. 1) (Bernier et al., 2011; Pagan et al., 2018; Poulsen, 2004; Suter et al., 2006). While being illuminated by a monochromatic X-ray beam, the sample is rotated, and the individual grains within the illuminated volume diffract as they satisfy Bragg's diffraction condition. HEDM employs area detectors to collect diffracted intensity as spots, where the positions of the spots upon the detector are informed by both the position of the diffracting volume within the sample and the orientation of the diffracting crystallographic planes. Far-field HEDM (FF-HEDM) captures the diffracted intensity upon detectors placed about a meter downstream of the sample. At such a far distance from the sample, the diffracted intensity's location upon the detector is dominated by the orientation of the diffracting volume, which gives FF-HEDM high angular resolution in orientation measurements of $\pm 0.01^{\circ}$ and elastic strain measurements of $\pm 1 \times 10^{-4}$ (Hurley et al., 2018; Schuren and Miller, 2011). Near-field HEDM (NF-HEDM) places the detector at a close distance, on the order of millimeters, downstream from the sample. With a close detector, the spatial resolution is greatly increased while the angular resolution is diminished, so that NF-HEDM provides $< \pm 0.1^{\circ}$ and 2 μm in orientation and spatial resolution, respectively (Li and Suter, 2013; Schuren et al., 2015; Suter et al., 2006). Thus, the FF-HEDM measurements are used to reconstruct grain-averaged centroids, orientations, elastic strain tensors with increased resolution in orientation, while the NF-HEDM measurements are used to reconstruct lattice orientation fields and grain morphology with enhanced spatial resolution. The data from the two data sets are then merged to build a complete picture of the microstructure and micromechanical evolution. We note that intragranular distribution of elastic strain, such as those that can be extracted from CPFE simulation, are not measured.

In the present work, the HEDM experiments are conducted at the Cornell High Energy Synchrotron Source's F2 beamline with a monochromatic X-ray beam energy of 61.332 keV. The FF-HEDM area detectors, two Dexela 2923 detectors with 3888× 3072 pixels each and 74.8 μ*m* pixel size, are placed 734 mm downstream of the sample. An 800 μ*m* tall region along the loading axis, roughly centered in the 1500 μ*m* gauge length, is scanned throughout the experiment via eight overlapping 120 μ*m* boxes and each FF-HEDM scan is reconstructed with HEXRD (Bernier et al., 2011). In the current experimental setup, the reconstructed elastic strain tensor from FF-HEDM is grain-averaged. For NF-HEDM, a LuAg:Ce scintillator paired with a 5x objective lens to a Retiga 4000DC CCD camera is placed 6.40 mm from the sample. The imaging setup results in 2048 × 2048 pixels with an effective pixel size of 1.48 μ*m*. NF-HEDM is conducted on the same 800 μ*m* region with similarly sized boxes and is reconstructed by seeding a forward-modeling based reconstruction method (Juul et al., 2016; Pagan et al., 2018) with FF-HEDM data and using a voxel spacing of 2 μ*m*. Thus, NF-HEDM resolution informs the mesh size for the CPFE simulation. However, in this work, the mesh is coarsened further for computational advantages (see Section 3.2 for details). The reconstructed microstructure of the material is shown in Fig. 2(a). After NF-HEDM is conducted, the sample is cycled to 1% macroscopic strain, then reverse loaded to 0% macroscopic strain and finally back to 1% macroscopic strain. FF-HEDM is conducted intermittently, a total of 11 times, over the same 800 μ*m* region (spatial registration is facilitated by tracking a metal wire glued to the sample's surface). FF-HEDM is conducted before and after the macroscopic yield point, at 0.8% and 1% macroscopic strain, at an unloaded state after 1% macroscopic strain, at the reverse proportional limit and 0% macroscopic strain. Additionally, FF-HEDM is conducted at an unloaded state upon reloading, and again at the proportional limit and 1% macroscopic strain. The cyclic loading is facilitated by the RAMS2 load frame (Shade et al., 2015). After reconstruction, the data from both NF-HEDM and FF-HEDM is integrated via a combination of DREAM.3D pipelines (Groeber and Jackson, 2014) and an in-house MATLAB script, and subsequently is visualized in ParaView.

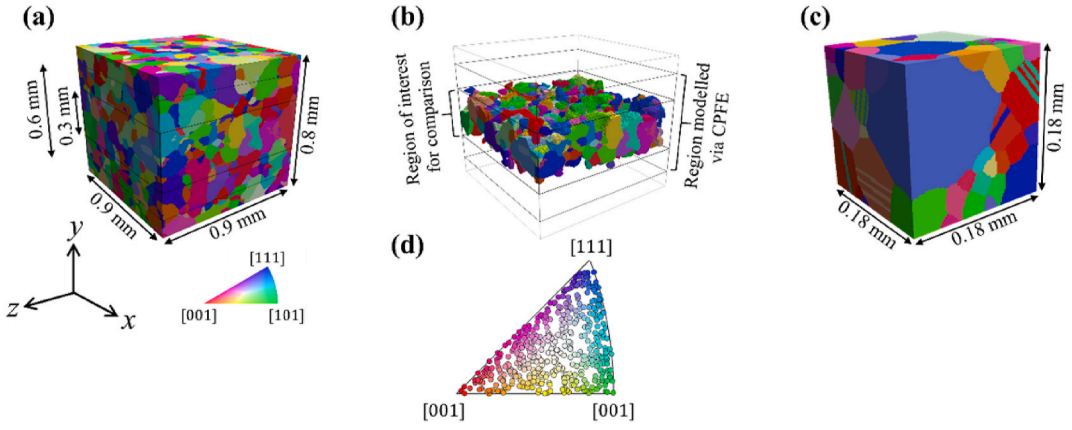

Fig. 2. (a) Reconstructed polycrystalline aggregate of 718Plus from NF-HEDM. (b) Grains within the region of interest for the comparison between the CPFE simulation and FF-HEDM experiment. (c) A statistically equivalent microstructure for 718Plus. (d) The orientation of the grains in part (b).

3. Crystal plasticity finite element simulation framework

In this work, the CPFE simulation framework is composed of three primary components: (a) kinematic and kinetic equations of the crystal plasticity model, (b) creation and discretization of a polycrystalline microstructural model for finite element simulations, and (c) estimation of the crystal plasticity model parameters for the subsequent analysis. Each of these items is described separately below.

3.1. Kinematics and kinetics of crystal plasticity

The crystal plasticity model, adopted in this work, is the extension of the phenomenological, rate-dependent formulation used by (Anand and Kothari, 1996; Asaro and Needleman, 1985; Kapoor and Sangid, 2018) and is implemented in a commercially available finite element software, ABAQUS, via a user material (UMAT) subroutine. The details of the model are as follows.

As described in Section 1, Eq. (1) relates the thermodynamic conjugate shear stress on the i^{th} slip system, i.e., π^i, to the resolved shear stress on the same slip system, i.e., τ^i. The term λ^i, in Eq. (1), represents the stretch ratio along the slip direction associated with the i^{th} slip system. In this work, we consider total strain ~1%, the stretch ratio is approximately one, i.e., $\lambda^i \approx 1$. Thus, Eq. (1) reduces to

$$\pi^i = \tau^i - \chi^i\left(\widehat{\mathbf{F}}, \gamma\right) \tag{9}$$

Further, for isothermal deformation, which is the case in the current work, the thermoelastic deformation gradient $\widehat{\mathbf{F}}$ reduces to the elastic deformation gradient, denoted by $\mathbf{F^E}$. Hence, using the notion of multiplicative decomposition (Clayton et al., 2014; Clayton and McDowell, 2003; Lee, 1969), the total deformation gradient $\mathbf{F}$ can be related to $\mathbf{F^E}$ and plastic deformation gradient $\mathbf{F^P}$ as (Kapoor and Sangid, 2018):

$$\mathbf{F} = \mathbf{F^E F^R F^P} \tag{10}$$

Here, $\mathbf{F^R}$ is introduced as an *Eigen deformation gradient* to provide a mathematical framework to initialize residual stress within the CPFE framework. Specifically, the residual elastic strain, $\boldsymbol{\varepsilon}$, is determined from the FF-HEDM experiments. Subsequently, based on the small strain assumption, the following equation is used to solve for the initial $\mathbf{F^E}$

$$\boldsymbol{\varepsilon} = \frac{1}{2}\left(\mathbf{F^{E^T}} + \mathbf{F^E}\right) - \mathbf{I} \tag{11}$$

Thus, initial $\mathbf{F^E}$ is not an identity tensor. However, the initial $\mathbf{F}$, as well as $\mathbf{F^P}$, should be the identity tensors, which cannot be achieved simultaneously in the absence of $\mathbf{F^R}$. Thus, the initial $\mathbf{F^E F^R}$ is an identity tensor, which, together with identity $\mathbf{F^P}$, makes the initial $\mathbf{F}$ an identity tensor. By initializing the residual stress, which has been shown to improve the match between the CPFE simulations and HEDM experiments (Kapoor and Sangid, 2018), the uncertainty in the results of the current analysis is minimized. The plastic velocity gradient, which relates the shearing rates on each slip system $\dot{\gamma}^i$, is calculated using the following equation (Rice, 1971):

$$\mathbf{L^P} = \dot{\mathbf{F}}^{\mathbf{P}}(\mathbf{F^P})^{-1} = \sum_{i=1}^{N_{sys}} \dot{\gamma}^i\left(\mathbf{s}_0^i \otimes \mathbf{n}_0^i\right) \tag{12}$$

with $\mathbf{s}_0^i$, $\mathbf{n}_0^i$, and $\dot{\gamma}^i$ being a unit vector along the slip direction, a unit vector along the slip plane normal, and the shearing rate for the i^{th}slip system, respectively. In Eq. (12), N_{sys} is the total number of slip systems. Since 718Plus is an FCC material, $N_{sys} = 12$, corresponding to the twelve ⟨110⟩{111} octahedral slip systems in the FCC materials. The flow rule, relating the shearing rate on a slip system to the thermodynamic conjugate shear stress (defined in Eq. (9)) is represented using a power law (Hutchinson, 1976) as follows:

$$\dot{\gamma}^i = \dot{\gamma}_0\left|\frac{\tau^i - \chi^i}{g^i}\right|^m \mathrm{sgn}\left(\tau^i - \chi^i\right) \tag{13}$$

where τ^i, g^i, and χ^i are the resolved shear stress, reference stress, and the backstress for the i^{th} slip system, respectively; $\dot{\gamma}_0$ and m are the reference shearing rate and the inverse strain rate sensitivity exponent, respectively. The evolution of the reference stress is based on an Armstrong-Frederick type equation and is given by (Horstemeyer et al., 1999; McGinty, 2001):

$$\dot{g}^i = H\sum_{j=1}^{N_{sys}} q^{ij}|\dot{\gamma}^j| - H_D g^i \sum_{j=1}^{N_{sys}} |\dot{\gamma}^j| \tag{14}$$

where H and H_D are the direct and dynamic recovery coefficients, respectively; q^{ij} is the hardening matrix such that the diagonal terms represent self-hardening and off-diagonal terms are associated with latent hardening ($q^{ij} = 1$ for diagonal terms and 1.2 for off-diagonal terms) (Kocks, 1970).

As discussed in Section 1, the current work investigates two backstress formulations: the empirical AF model and the

phenomenological GND-based model. The mathematical description of both models is presented in Section 1. However, for the sake of completeness and continuity, we reproduce those equations here again. In AF-type model (Armstrong and Frederick, 1966), backstress evolves as

$$\dot{\chi}^{i} = A\dot{\gamma}^{i} - A_{D}\chi^{i}|\dot{\gamma}^{i}| \tag{15}$$

where A and A_D are the direct hardening and dynamic recovery coefficients, respectively. In the GND-based description (Kapoor et al., 2018), the backstress is computed at the beginning of every time step using

$$\chi^{i} = K\mu b^{i}\sqrt{\rho^{i}_{GND}} \tag{16}$$

where b^i and ρ^i_{GND} are the Burgers vector and the GND density for the i^{th} slip system; K is a scaling constant, and μ is the isotropic shear modulus of the material. The calculation of GND densities is carried out at the end of each time step by equating the dislocation density tensor to the open Burgers circuit as follows (Acharya and Bassani, 2000; Arsenlis and Parks, 1999; Dunne et al., 2012; Nye, 1953):

$$\sum_{i=1}^{N}\rho^{i}_{GND}\mathbf{b}^{i}\otimes\mathbf{t}^{i} = \mathrm{Curl}\left(\mathbf{F}^{\mathbf{P}}\right) \tag{17}$$

where $\mathbf{t}^i$ is the tangent vector for the i^{th} GND type. The calculation of GND densities is carried out at the end of every time step using Eq. (17), by leveraging finite element shape functions, based on the work by Kapoor et al. (2018) and kept constant for a time step.[3] A fully implicit method with incremental line search algorithm and time step subincrementation is used to compute $\dot{\gamma}^i$ in Eq. (13) for each time step (McGinty, 2001).

3.2. Discretized polycrystalline microstructures

To compare the simulated stress values with the same obtained from the HEDM experiments, the microstructure model for CPFE simulations should correspond to the exact material volume interrogated during the HEDM experiments. To this end, the microstructure model for simulation is directly obtained from the NF-HEDM reconstruction, as described in Section 2.2. Since the reconstructed sample has a 900 $\mu m \times 900\ \mu m$ cross-sectional area (removing material from the free surface representing a high degree of uncertainty during the reconstruction process) at the gauge section and a total of 800 μm region is interrogated along the loading axis during the HEDM experiments, the reconstructed microstructure (see Fig. 2(a)) has dimensions of $900\ \mu m \times 900\ \mu m \times 800\ \mu m$. To make the CPFE simulations tractable, only a 600 μm region, centered within the 800 μm interrogated region, is modeled (see Fig. 2(a)) in this work. Further, to eliminate any effect of the imprecise boundary conditions[4] on the simulated response and thereby the simulation-experiment comparison, the reported results are restricted to a 300 μm region in the middle of the simulated polycrystalline aggregate containing 508 grains (see Fig. 2(b)). As evident in Fig. 2(d), these 508 grains show a random texture.

As described in Section 2.2, the HEDM experiments are carried out until one and a half cycles of cyclic loading. To identify the similarities and differences between the response from the two backstress models, it is necessary to carry out CPFE simulations for additional cycles of loading. Due to the substantial size of the microstructure in Fig. 2(a), even after removing 100 μm of the simulation domain from the top and the bottom, it is practically infeasible to run simulations involving a large number of loading steps in a reasonable amount of time. Hence, another microstructure, which is smaller in size ($180\ \mu m \times 180\ \mu m \times 180\ \mu m$) but representative of the 718Plus microstructural statistics (e.g., grain size and orientation distribution), is created[5] using a framework that is described in detail elsewhere (Bandyopadhyay et al., 2019; Bandyopadhyay and Sangid, 2019; Prithivirajan and Sangid, 2018, 2020). The resulting microstructure model, referred to as a statistically equivalent microstructure, is shown in Fig. 2(c).

In this work, the GND-based backstress description (see Eq. (8) or (16)) is mesh-dependent. Specifically, the computation of the GND density, i.e., ρ^i_{GND}, requires numerical evaluation of the derivatives within the $\mathrm{Curl}(\mathbf{F}^{\mathbf{P}})$ term (see Eq. (17)). Hence, the scaling constant K is introduced within the GND-based backstress definition to scale the $\mu b^i\sqrt{\rho^i_{GND}}$ term to result in realistic backstress magnitudes at the length-scale of finite element mesh. Thus, the scaling constant K is also mesh-dependent, and it is crucial to choose an appropriate mesh size to carry out CPFE simulations. Based on a mesh sensitivity analysis performed by Prithivirajan and Sangid (2018) on the AF model, we choose an element size of 3 μm. With this, both NF-HEDM and statistically equivalent microstructures are discretized using $3\ \mu m \times 3\ \mu m \times 3\ \mu m$ hexahedron elements within DREAM.3D software (Groeber and Jackson, 2014). Once the mesh size is fixed, the scaling constant K is obtained using a genetic algorithm framework, as described in Section 3.3. Also, it is to be noted

[3] It is necessary to choose considerably small time increments for the GND-based backstress model, compared to the AF-type model, for numerical convergence.

[4] During CPFE simulations, y-component of the displacement was set to zero at the bottom face of the microstructure model (see Fig. 2(a)) and a non-zero y-component of displacement, consistent with experimentally applied strain on the specimen (see Fig. 1), was specified on the top face as boundary conditions.

[5] From an electron backscatter diffraction characterization of 718Plus, twin area fraction in the material was found to be ~0.5. Hence, twins were inserted in the smaller microstructure, as shown in Fig. 2(c), using a methodology described in (Chan, 2010).

that the mesh size within the NF-HEDM, as well as the statistically equivalent microstructures, is the same, which allows us to use the same scaling constant K for both microstructure models during CPFE simulations.

3.3. Crystal plasticity parameter estimation

In the present research, there are two CPFE simulation frameworks – one using the AF-type backstress model and another using the GND-based backstress description. Let, $\boldsymbol{\theta}_{AF}$ and $\boldsymbol{\theta}_{GND}$ be the sets representing the unknown crystal plasticity model parameters in these two frameworks, i.e., $\boldsymbol{\theta}_{AF} = \{\dot{\gamma}_0, m, g_0, H, H_D, \chi_0, A, A_D\}$ and $\boldsymbol{\theta}_{GND} = \{\dot{\gamma}_0, m, g_0, H, H_D, K\}$, where g_0 and χ_0 are the initial values of g^i and χ^i, respectively. Since $\dot{\gamma}_0$ and m are associated with strain rate sensitivity of the slip systems, and g_0 is associated with the initial critical resolved shear stress of the material, these three parameters should numerically be identical in $\boldsymbol{\theta}_{AF}$ and $\boldsymbol{\theta}_{GND}$. On the other hand, the description of g^i and χ^i in both frameworks are coupled via $\dot{\gamma}^i$ (see Eqs. 12–17). Hence, to ensure identical macroscopic response from these two CPFE frameworks, H and H_D values are likely to be different in $\boldsymbol{\theta}_{GND}$ from $\boldsymbol{\theta}_{AF}$ because of different types of backstress formulations and associated model parameters. Here, we fit the parameters in $\boldsymbol{\theta}_{AF}$ to the experimentally obtained macroscopic stress-strain data of 718Plus using a genetic algorithm based optimization routine (Bandyopadhyay et al., 2019; Prithivirajan and Sangid, 2018). Since this fitting is computationally expensive, we use the fitted H and H_D values from $\boldsymbol{\theta}_{AF}$ in $\boldsymbol{\theta}_{GND}$ and adjust the parameter K in $\boldsymbol{\theta}_{GND}$ to match the simulated macroscopic stress-strain response from the GND-based CPFE framework to the experimental data. One could, in principle, have fitted $\boldsymbol{\theta}_{GND}$ first and subsequently adjusted A and A_D in $\boldsymbol{\theta}_{AF}$. However, this approach would lead to even higher computation cost due to the computation of $\mathrm{Curl}(\mathbf{F}^P)$ and solution of ρ^i_{GND} in Eq. (17). Hence, the second approach is avoided here.

The fitting of $\boldsymbol{\theta}_{AF}$ is posed as a minimization problem, where the objective function, $f(\boldsymbol{\theta}_{AF})$, is given by:

$$f(\boldsymbol{\theta}_{AF}) = \sqrt{\frac{1}{N}\sum_{j=1}^{N}\left(1 - \frac{S^j_{sim}(\boldsymbol{\theta}_{AF})}{S^j_{exp}}\right)^2} \tag{18}$$

Here, S^j_{exp} is the experimental (macroscopic) stress value and $S^j_{sim}(\boldsymbol{\theta}_{AF})$ is the microstructure averaged simulated stress in the loading direction corresponding to the j^{th} point on the macroscopic stress-strain curve and N is the total number of points chosen along the macroscopic stress-strain curve. The anisotropic elastic constants and fitted crystal plasticity parameters for 718Plus are reported in Table 1. The fitted parameter values in $\boldsymbol{\theta}_{AF}$ are consistent with previous work (Bandyopadhyay et al., 2020). Simulated macroscopic stress-strain response using the parameters in Table 1 is compared with the experimental stress-strain response of 718Plus in Fig. 3. To fit the crystal plasticity parameters and generate the plots in Fig. 3, the statistically equivalent microstructure model in Fig. 2(c) has been used.

In Fig. 3, one might notice that the GND-based backstress model (macroscopically) shows almost linear hardening after yielding in compression. Since, in addition to the kinematic hardening parameters, the post-yield shape of the macroscopic stress-strain curve is significantly influenced by H and H_D, such an observation supports the preceding discussion that one would need to fit H, H_D, and K simultaneously for the GND-based CPFE framework. In this paper, we keep H and H_D to be the same in both CPFE frameworks to isolate the differences in the micromechanical response solely due to the difference in kinematic hardening descriptions.

For a given set of experimental macroscopic stress-strain data, the parameter values in Table 1 are not unique, which might lead to uncertainty in the subsequent CPFE analysis. In related work, the authors quantified the variability associated with each parameter in $\boldsymbol{\theta}_{AF}$ in terms of coefficient of variation for another material system, namely, IN718 (Bandyopadhyay et al., 2019). It was observed that the uncertainty in the simulated stress along the loading direction due to the variability associated with the crystal plasticity parameters was path-dependent and bounded by ~10% of the maximum stress value in the macroscopic stress-strain diagram, i.e., ~100 MPa is this work, (Bandyopadhyay et al., 2019). The implication of such uncertainty in this work is discussed further in Section 4.2.

4. Results and discussions

4.1. Stress analysis from HEDM

The evolution of the grain-averaged stresses in the loading direction along the macroscopic loading path (see Fig. 4(a)), within the

Table 1
Anisotropic elastic constants and the calibrated crystal plasticity parameters.

Parameter	Value	Parameter	Value
C_{11}	239.57 GPa	H	1885 MPa
C_{12}	141.18 GPa	H_D	8
C_{44}	107.04 GPa	A	5997 MPa
$\dot{\gamma}_0$	4.25×10^{-4} s^{-1}	A_D	31
m	12	χ_0	10.2 MPa
g_0	290.3 MPa	K	0.4
μ	77.2 GPa	b	3.52 Å

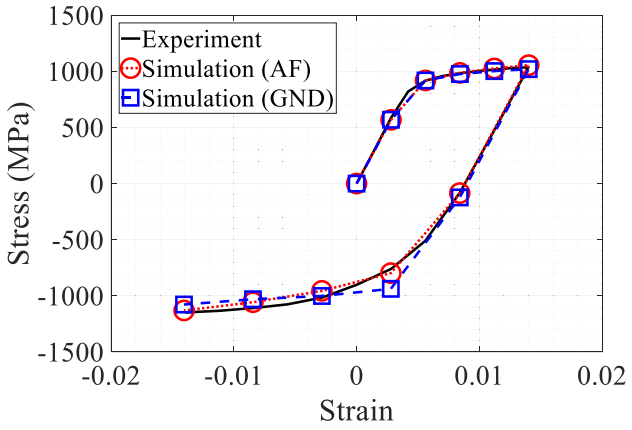

Fig. 3. Comparison between the simulated and experimental macroscopic stress-strain response of 718Plus.

region of interest from the HEDM reconstruction, is shown in Fig. 4(b). At state 1, the specimen is not loaded macroscopically. However, one can observe a heterogeneous (type II) residual stress distribution within the microstructure, which originates from the material's processing. With the increase in macroscopic loading, the stress within each grain increases monotonically, as expected, until state 5. While unloading, although the specimen is under tension, macroscopically, from states 5 to 6, many grains within the region of interest transition from a tensile to compressive stress state before reaching state 6. Consequently, at state 6, one can observe a combination of tensile-compressive grain-averaged stresses within the microstructure leading to an overall zero stress for the polycrystalline aggregate. From a mechanistic standpoint, such a non-uniform transitioning from a tensile to compressive stress state is a direct consequence of the non-uniform evolution of the internal variable backstress within each grain during loading from states 1 to 5. Moreover, such a non-uniform stress-state transitioning at the grain level or mesoscopic length-scale is manifested as early macroscopic yielding during subsequent compressive loading, which is typically referred to as the Bauschinger effect in the literature. In the present work, the Bauschinger effect can be observed in the macroscopic stress-strain curve, as shown in Fig. 4(a), wherein yielding in compression is observed around state 7, which is associated with a much lower stress magnitude compared to state 2.

With the increase in compressive load magnitude after state 6, the compressive stress within each grain continues to increase monotonically from states 6 to 8. While returning to zero load after state 8, the specimen is nominally under compression from state 8 to 9. However, a large number of grains transitions from compression to tension before reaching state 9. Consequently, at state 9, a combination of tensile-compressive stresses is observed, resulting in an overall zero average stress across the region of interest. As previously mentioned, such a non-uniform transitioning from compression to tension is a direct consequence of non-uniform kinematic hardening for each grain developed during the preceding loading path. With the further increase in macroscopic loading, the stress within the grains continues to increase monotonically until state 11.

In Fig. 4(b), it is interesting to observe that although the material is nominally under zero load at states 1, 6, and 9, the stress distributions within the region of interest at these states are qualitatively as well as quantitatively different from each other. To illustrate this observation further, in Fig. 5, we compare the stress experienced by each grain within the region of interest in the loading direction at states 1, 6, and 9. Precisely, stress values at states 6 and 9 are plotted against the stress values at states 1 and 6 in Fig. 5(a) and (b), respectively. From Fig. 5, it is evident that the same set of grains experience qualitatively (tension vs. compression) as well as quantitatively (lower vs. higher magnitude) different stress at the nominally zero macroscopic load states. The data points in the shaded quadrants in Fig. 5 indicate the grains that transition from tension to compression (bottom right quadrant) or compression to tension (upper left quadrant) as we move from state 1 to 6 (Fig. 5(a)) or state 6 to 9 (Fig. 5(b)), whereas the grains in the unshaded quadrants only experience a change in stress magnitude. Such an observation is not surprising, rather reinforcing the fact that the stress state within the microstructure, during elasto-plastic deformation involving macroscopic load reversals, is inherently dependent on loading history.

From the results, as presented above, it is evident that the present experiment not only reproduces the Bauschinger effect at the macroscopic length-scale, but also captures corresponding events at the mesoscopic length-scale via heterogeneous (average) stress response of the individual grains. Crystal plasticity models are inherently capable of capturing the material response at such a length-scale. Thus, the present HEDM dataset offers rich information to assess the performance of two different kinematic hardening models via comparing stress response at the mesoscopic length-scale.

4.2. Comparison between the HEDM and crystal plasticity responses

In Figs. 6 and 7, the grain-averaged stresses in the loading direction, for the grains identified in Fig. 2(b), from the HEDM reconstruction are compared to the same from CPFE simulations with AF and GND-based backstress descriptions, respectively. Within each subplot of Figs. 6 and 7, ζ represents an estimate of the mismatch between the experimental data and model predictions and is

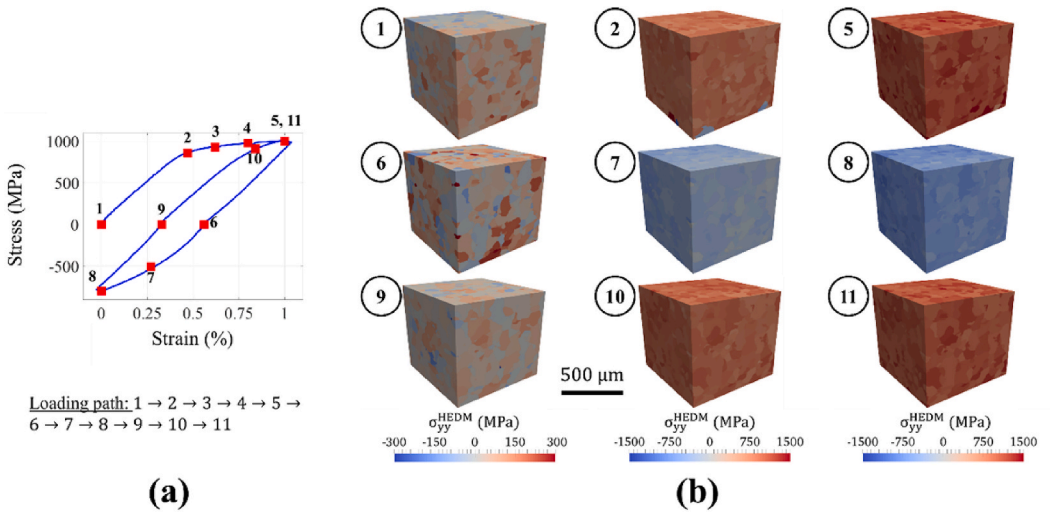

Fig. 4. (a) Probed deformation states via HEDM experiments along the macroscopic loading path. (b) Grain-averaged stress values in the loading direction, i.e., σ_{yy}^{HEDM}, within the reconstructed microstructure of 718Plus at selected probed states, as indicated in part (a).

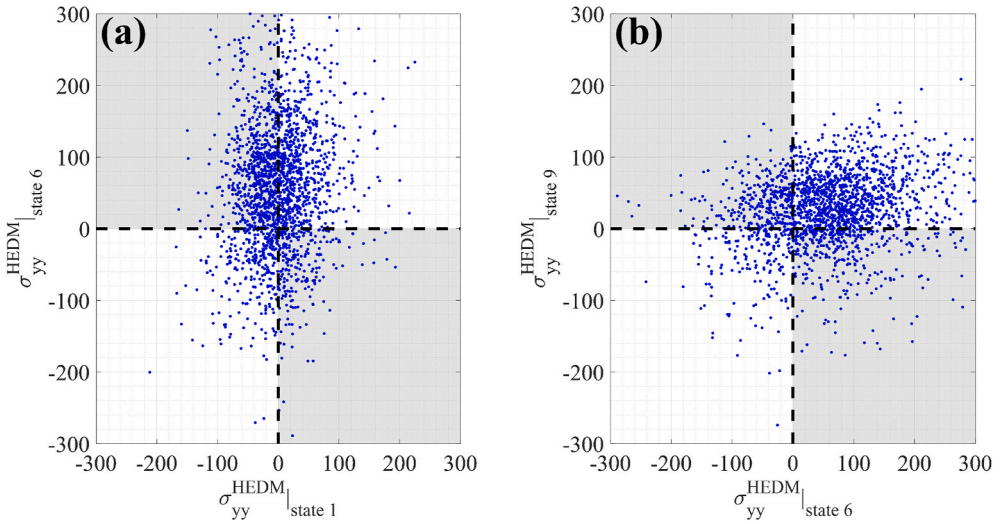

Fig. 5. Comparison of stress in the loading direction from HEDM reconstruction at nominally zero load states 1 and 6 (part (a)), and 6 and 9 (part (b)).

defined by

$$\zeta = \sqrt{\sum_{k=1}^{508} \frac{\left(\sigma_{yy}^{AF \text{ or } GND}\Big|_k - \sigma_{yy}^{HEDM}\Big|_k\right)^2}{508}} \tag{19}$$

In Eq. (19), the summation and the averaging are performed over 508 grains as shown in Fig. 2(b); $\sigma_{yy}^{HEDM}\Big|_k$ is the grain-averaged stress in the loading direction within the k^{th} grain from HEDM experiments; $\sigma_{yy}^{AF \text{ or } GND}\Big|_k$ is the grain-averaged stress in the loading direction within the same grain from CPFE simulations using either AF (Fig. 6) or GND-based (Fig. 7) backstress model. In the event of perfect agreement between experimental and simulated responses, all data points would lie on the dashed reference line. However, in both Figs. 6 and 7, one can observe the data points are distributed about the reference line. In particular, the models overpredict (or underpredict) the stresses for the data points lying above (or below) the reference line.

The disagreement between the experimental and simulated responses can be attributed to the errors originating from the HEDM experiments, as well as CPFE simulations. For HEDM measurements performed at CHESS, an error of $\pm 1 \times 10^{-4}$ is reported in strain measurements (Hurley et al., 2018) that would lead to about ±50 MPa error in stress calculations for the present set of elastic

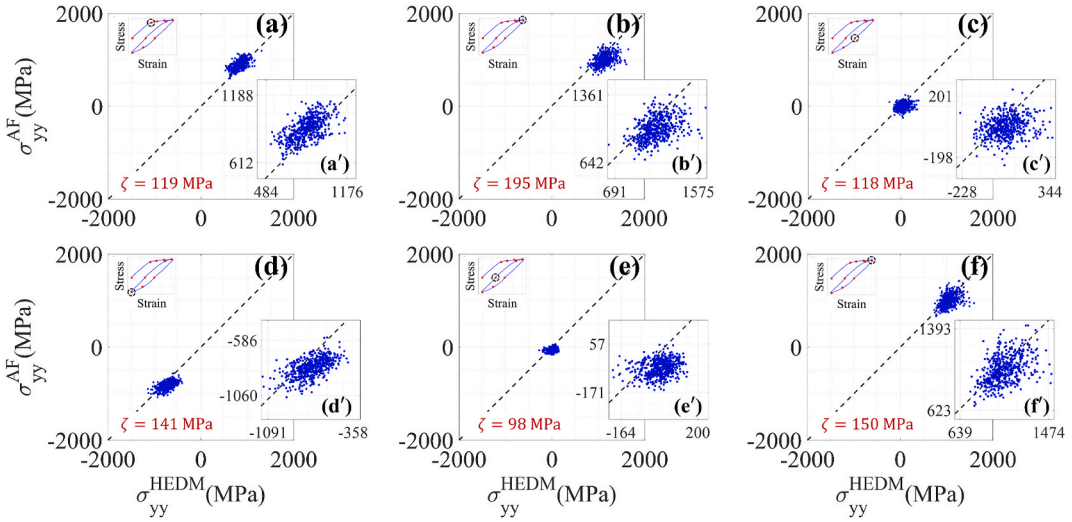

Fig. 6. (a)–(f) Comparison of the grain-averaged stress obtained from FF-HEDM experiments (σ_{yy}^{HEDM}) and CPFE simulations using the AF backstress model (σ_{yy}^{AF}). (a')–(f') Magnified view of data points in part (a)–(f). ζ represents an estimate of the mismatch between the experimental data and model predictions and is defined in Eq. (19).

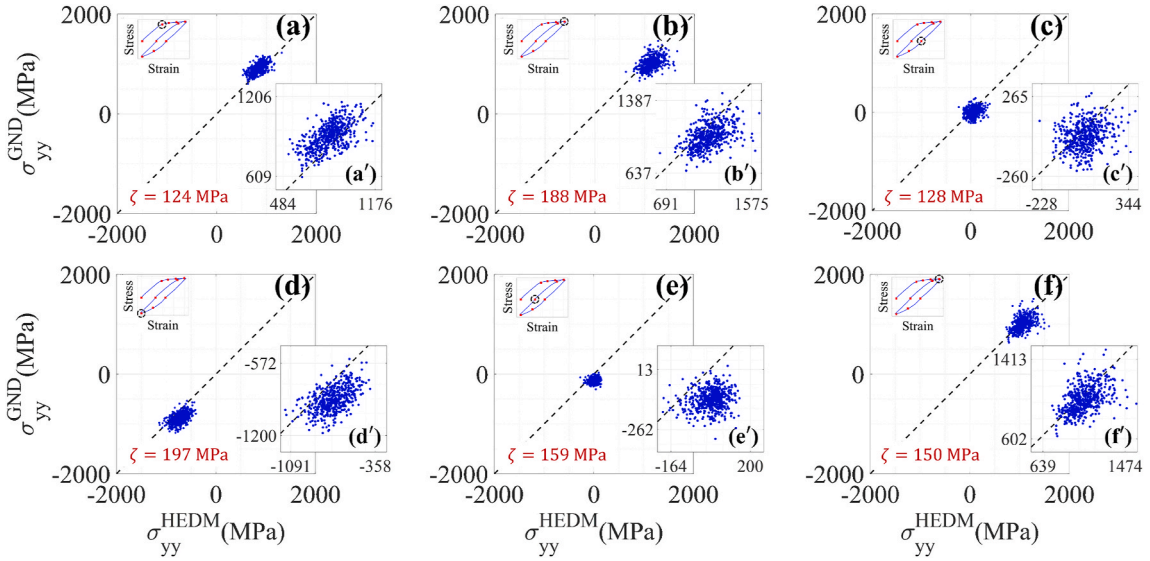

Fig. 7. (a)–(f) Comparison of the grain-averaged stress obtained from FF-HEDM experiments (σ_{yy}^{HEDM}) and CPFE simulations using the GND-based backstress model (σ_{yy}^{GND}). (a')–(f') Magnified view of data points in part (a)–(f). ζ represents an estimate of the mismatch between the experimental data and model predictions and is defined in Eq. (19).

constants. On the other hand, for a given set of constitutive equations, the uncertainty in the CPFE simulation results is dominated by imprecise crystal plasticity parameters. In Section 3.3, it is mentioned that the parameter values in Table 1 are not necessarily unique when these are fitted to the macroscopic stress-strain response of the material. For IN718 and AF-type backstress model, Bandyopadhyay et al. quantified the variability associated with the crystal plasticity parameters (Bandyopadhyay et al., 2019). Subsequently, they showed that the uncertainty in the stress along the loading direction, originating due to the variability associated with the crystal plasticity parameters, is path-dependent, which implies that the coefficient of variation in the stress along the loading direction is not the same at the state points in Fig. 4(a). In their analysis, the maximum coefficient of variation was ~0.1, which gives us an *engineering estimate* of the bounds associated with the uncertainty in the stress along the loading direction from CPFE simulations. Here, since the maximum stress in the loading direction is ~1000 MPa, we may expect an error up to ±100 MPa in the simulated stress values in the loading direction due to the non-uniqueness associated with the crystal plasticity parameters in Table 1. With these limitations in the experiment as well as simulation, both kinematic hardening models capture the experimental data decently in an average sense.

To better understand the degree of (dis)agreement between the two kinematic hardening descriptions, a similar stress comparison

plot is shown in Fig. 8. Within each subplot in Fig. 8, ζ follows a similar definition, as in Eq. (19), with $\left(\sigma_{yy}^{\text{AF or GND}}\Big|_k - \sigma_{yy}^{\text{HEDM}}\Big|_k\right)^2$ being replaced by $\left(\sigma_{yy}^{\text{AF}}\Big|_k - \sigma_{yy}^{\text{GND}}\Big|_k\right)^2$. Fig. 8(a) shows that both models produce identical grain-averaged stress response at the onset of macroscopic yielding, which is because the backstress values do not significantly evolve, on average, within the microstructure before the macroscopic yielding. In the subsequent loading states, one can observe progressive disagreement between the responses of the two backstress models, which confirms that two kinematic hardening descriptions, in the present work, capture the evolution of backstress in the individual grains differently. Although the axial component of the stress tensor in the loading direction, i.e., σ_{yy}, is plotted in Figs. 6–8, the remaining components have also been examined and show similar (dis)agreement.

From Figs. 6–8, with particular focus on the ζ values, one would probably infer that there is either no or marginal improvement in the CPFE results from the GND-based backstress model. However, it is perhaps unfair to expect a radical improvement in the simulated stress response at all states along a macroscopic stress-strain curve, by adopting a better backstress model. As mentioned before, Bandyopadhyay et al. (2019) showed that the uncertainty in the stress along the loading direction from the CPFE simulations is path-dependent, i.e., the uncertainty is different at different macroscopic state points. They also showed that all crystal plasticity parameters do not contribute equally to the overall uncertainty at different state points on a macroscopic stress-strain curve and the contribution of one or a set of parameters to the overall of uncertainty is consistent with their physical relevance at that state point. In the present context, it implies that one may not necessarily expect a radical improvement in the simulation results at all states. In other words, one would expect appreciable improvement in the simulated response at states 6, 7, and 8 because these are associated with the Bauschinger effect. To elucidate this further, the grain-averaged stresses in the loading direction within the grains, as identified in Fig. 2(b), are plotted against grain size for loading states 5, 6, 8, 9, and 11, in Fig. 9. While generating Fig. 9, the mean stress of the set of grains has been shifted to zero to focus only on the associated scatter. To help the reader better visualize, each cluster of data points in Fig. 9 is enclosed by a Gaussian envelope having zero mean and standard deviation equal to three times the standard deviation of the stress distribution of the corresponding data cluster. Such an envelope is referred to as a 'scatter envelope' in Fig. 9(d), (h), (l), (p), and (t). At state 5, both models produce an almost identical response, which is slightly different from the experimental measurement. At state 6, the response from the GND model is in better agreement with the HEDM results than the AF model, especially for the smaller grains. A similar trend is also observed in states 8 and 9. However, at state 11, both backstress models produce an almost identical response, which is in near-perfect agreement with the experimental values. Physically, the backstress or long-range internal stress is expected to develop inside the microstructure of the material during the formation of dislocation structures and substructures. The backstress in the simulation will evolve significantly if the shearing rate (i.e., $\dot{\gamma}^i$) is significant (for the AF model) or the plastic deformation gradient (i.e., $\mathbf{F^P}$) is large (for the GND model). In essence, both requirements imply that the backstress at the grain level will evolve only during significant plastic deformation. Now, the plastic deformation of an individual grain is influenced by its orientation with respect to the loading direction, size, morphology, and the response of the surrounding grains. Hence, it is expected that grains having similar dimensions but positioned within varying neighborhoods and having different orientations would experience varying levels of plasticity. Consequently, the evolution of the backstress and hence the evolution of the stress in the cyclic loading direction will also be significantly scattered. From Fig. 9, it is seen that the GND-based backstress description better captures such

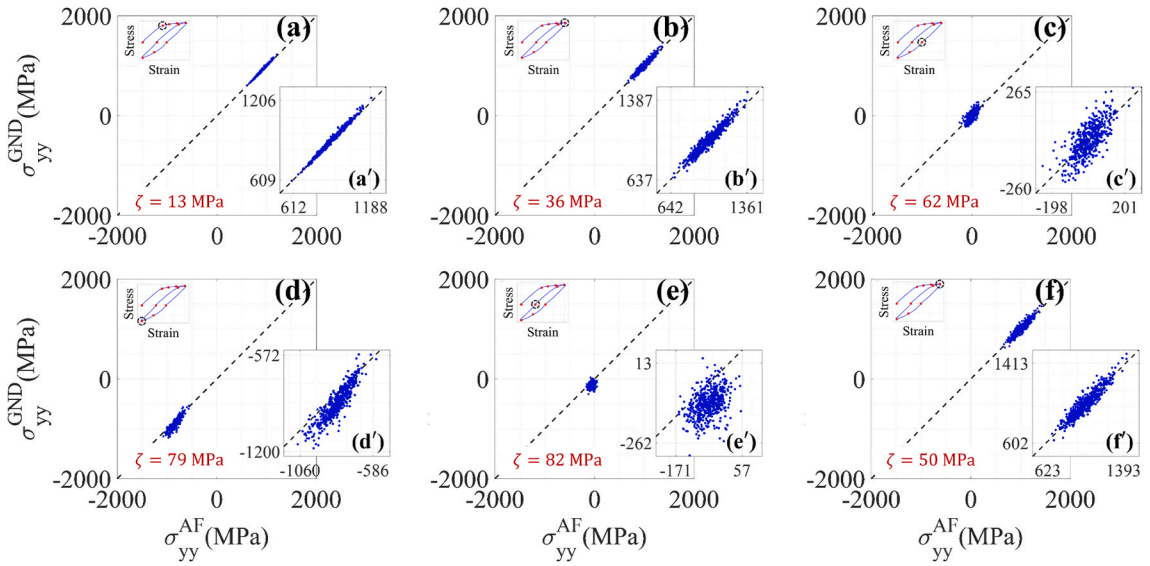

Fig. 8. (a)–(f) Comparison of the grain-averaged stress obtained from CPFE simulations using AF (σ_{yy}^{AF}) and GND-based (σ_{yy}^{GND}) backstress models. (a')–(f') Magnified view of data points in part (a)–(f). ζ represents an estimate of the mismatch between two model predictions, and follows a similar definition, as in Eq. (19), with $\left(\sigma_{yy}^{\text{AF or GND}}\Big|_k - \sigma_{yy}^{\text{HEDM}}\Big|_k\right)^2$ being replaced by $\left(\sigma_{yy}^{\text{AF}}\Big|_k - \sigma_{yy}^{\text{GND}}\Big|_k\right)^2$.

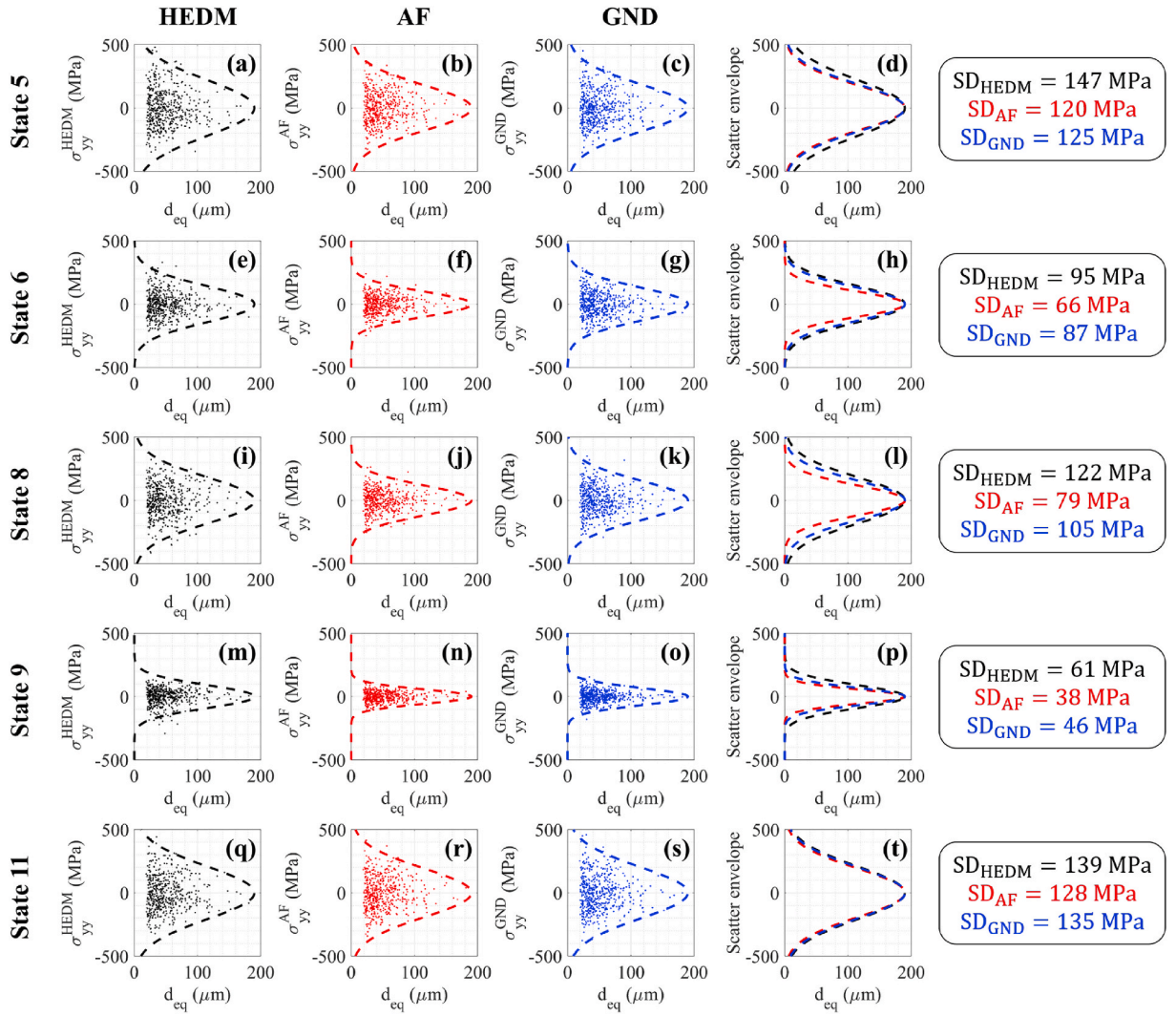

Fig. 9. Comparison of experimentally characterized grain-averaged stress heterogeneity to those obtained from CPFE simulations using the AF and GND-based backstress models at different deformation states along the macroscopic loading path indicated in Fig. 4(a). SD denotes standard deviation.

scattered behavior at the loading steps that are associated with the Bauschinger effect at the macroscopic length-scale. Quantitatively, the GND-based backstress model improves standard deviation (SD in Fig. 9) by ~72% and ~60% at states 6 and 8, respectively. Such a verification supports the preceding discussion on the expected improvement in the stress along the loading direction from a better backstress model.

5. Additional discussions

In the present work, HEDM experiments are continued until one and a half cycles, which give us ample information to investigate multiple macroscopic states within a cycle and show how the GND-based backstress model better captures the deformation heterogeneity, associated with cyclic plasticity, compared to the AF model. Further validation of the GND-based backstress model would require direct comparison of the cyclic evolution of σ_{yy}^{GND} to σ_{yy}^{HEDM}, which is left as future work. However, it is well-known that it takes hundreds of cycles to form stable dislocation structures and substructures that lead to long-range internal stress or backstress (Huang et al., 2008; Wang et al., 1984; Wang and Mughrabi, 1984), which allows us to explore if the GND-based model leads to a realistic evolution of the backstress with continued cyclic loading. To this end, the statistically equivalent microstructure model in Fig. 2(c) is subjected to 30 cycles of loading with 1% maximum strain at strain ratios of 0 and -1. The evolution of the backstress at strain ratio 0 is shown in Fig. 10, and the same for strain ratio −1 is shown in Fig. 11.

In Figs. 10 and 11, backstress values are similar from both models after the first load cycle. However, the GND-based model shows a monotonically increasing backstress for both loading conditions, whereas the AF model shows saturation around ten cycles. It is well-

known in the classical, as well as crystal plasticity, literatures that the AF model breaks down for non-symmetric loading conditions (Chaboche, 1991; Chaboche and Nouailhas, 1989a, 1989b; Hennessey et al., 2017; McDowell, 1995; Ohno and Wang, 1993a, 1993b; Schäfer et al., 2019). However, there exists a notion that the AF model performs reasonably well at a fully reversed load. In Fig. 10(b), it is evident that the backstress from the AF model does not shakedown to a near-zero value, as in Fig. 9(b). However, as can be verified from Fig. 10(a), the backstress from the AF model saturates[6] around ten cycles, which is unrealistic. Hence, the AF model may be a reasonable choice for symmetric loading conditions in J_2 plasticity, but may not be appropriate in the crystal plasticity constitutive modeling. The unrealistic shakedown and saturation behavior of the AF model leads to crystal plasticity simulations with stable hysteresis loops or non-evolving micromechanical fields after only a few loading cycles. Whereas, in engineering materials, especially Nickel-base superalloys, the hysteresis loops, and micromechanical fields continue to evolve for approximately a hundred cycles (Sangid et al., 2011).

Although loading is continued up to 30 cycles for the results presented in Figs. 10 and 11, Kapoor et al. showed that the backstress from the GND-based model continued to evolve until the 100th cycle for 0.05 stress ratio cyclic loading (Kapoor et al., 2018). With this, it is evident that the GND-based model leads to a more realistic evolution of the backstress. In crystal plasticity, other researchers adopted alternative backstress formulations (Hennessey et al., 2017; Schäfer et al., 2019), such as the Ohno-Wang model and Chaboche model, which also show realistic evolution of backstress. However, these models are empirical and involve material constants that cannot be currently measured/calibrated using experiments, which would eventually lead to higher uncertainty in the analysis, as discussed in Section 1. On the other hand, the GND-based model, in the present work, is physics-based, involves only one parameter, produces a physically realistic cyclic evolution of backstress, and amenable for further improvement, if necessary, as discussed below.

In Section 1, it has been mentioned that a lack of experimental validation of the crystal plasticity constitutive equations inhibits a practitioner from developing trust in the results of CPFE, which prevents these CPFE simulations for more widespread adoption within modern engineering workflows. In the context of kinematic hardening description, the HEDM experimental data not only enables one to choose the most accurate model but also provides a means to check consistency between the diffraction measurements and the GND-based backstress model. The diffraction spots in the HEDM experiments spread with progressive cyclic loading along the radial as well as azimuthal directions on the detector. The spot spreading along the azimuthal direction is associated with evolved misorientation within a grain (Naragani et al., 2019; Obstalecki et al., 2014; Pagan and Miller, 2014). Again, misorientation within a grain is associated with the GND density in that grain (Mughrabi, 2006; Mughrabi and Ungár, 2006; Ungar et al., 1984). Since the spot spreading can be tracked with cyclic loading, one can, in principle, track the GND density and thereby backstress via Eq. (16) with cyclic loading at different locations within the material. Thus, multi-modal information in HEDM experiments offers a path forward to improve the form of the GND-based backstress equation, if necessary, for more complex as well as new material systems. With this, it is evident that unlike other kinematic hardening models, the GND-based backstress model is amenable to be validated and verified via characterization of the internal state variables, associated with the model, using suitable experiments, which will eventually take the crystal plasticity models one step closer towards incorporation in the modern engineering workflows.

In Fig. 3, we have previously noticed that the GND-based backstress model (macroscopically) shows almost linear hardening after yielding in compression. In addition to the imprecise H and H_D values in $\boldsymbol{\theta}_{GND}$ (see discussion in Section 3.3), such an observation perhaps indicates limitations associated with the GND-based model. Although the GND-based model is promising based on the physical basis that informed its construction and the results shown in Figs. 9–11, further improvements might be necessary (potentially to the model form and/or model parameters). To this end, in future research, both cyclic evolution of the stress and diffraction spots from HEDM experiments would provide information to validate and/or improve the GND-based backstress model, as per the above discussion.

Finally, it is necessary to note that the implementation of the GND-based backstress model in an ABAQUS UMAT subroutine restricts the applicability of the model only for finite elements having more than one integration point because of the computation of the Curl term on the right-hand side of Eq. (17). In particular, for the present work, the GND-based model is implemented in an ABAQUS UMAT subroutine, considering hexahedron or linear brick elements, which have eight integration points per element. Linear brick elements are well-suited for meshing in a broad class of problems. However, such elements may not be the ideal choice in certain situations. For example, defects often originate from manufacturing processes (such as pores from additive manufacturing) or inherent chemical compounds within an alloy (such as inclusions present in many structural engineering alloys). In microstructure-sensitive response analyses at the mesoscopic length-scale under cyclic loading, it is crucial to preserve the morphology of such defects during meshing so that gradients in the mechanical field variables across interfaces can be captured faithfully. It is well-known that triangular elements in 2D and tetrahedral elements in 3D do an excellent job in these regards at a reasonably small number of finite element nodes compared to the rectangular elements in 2D or brick elements in 3D. However, the triangular elements in 2D or tetrahedral elements in 3D only have one integration point per element, and the GND-based model cannot be used for these elements. One can preserve the defect morphology with sufficiently small rectangular elements in 2D or brick elements in 3D, which would eventually lead to more computation cost. Therefore, depending on the criticality of the analysis, one needs to decide if preserving feature morphology is more critical than an accurate description of the kinematic hardening. Since computing power is increasing at a

[6] One can possibly argue that a different set of Aand $A_D$would result in a different saturation speed and value of the backstress, but the choice of Aand $A_D$cannot be arbitrary. Given the nonlinear nature of the crystal plasticity equations, one may pursue a better set of backstress parameters. From a practical standpoint, such an effort does not help a practitioner build trust in the form of the model equations and solve real-life engineering problems. As we emphasize in Section 1, one of the possible avenues to build confidence in the CPFE framework is to choose models that are physics-based and involve the least number of parameters. Towards that direction, the GND-based backstress model is promising.

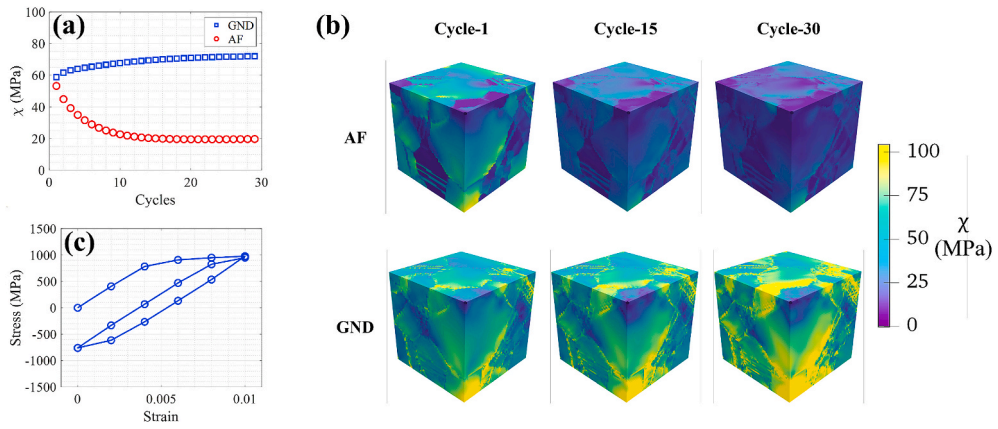

Fig. 10. (a) For $R_\varepsilon = 0$ loading, cyclic evolution of the backstress at a point within the microstructure, where the maximum value of the backstress, out of all twelve slip systems, is highest within the microstructure after the first cycle. (b) Cyclic evolution of the maximum value of backstress, out of all twelve slip systems, within the microstructure. (c) Macroscopic stress-strain response of the microstructure until one and a half cycles for the simulated loading condition in parts (a) and (b).

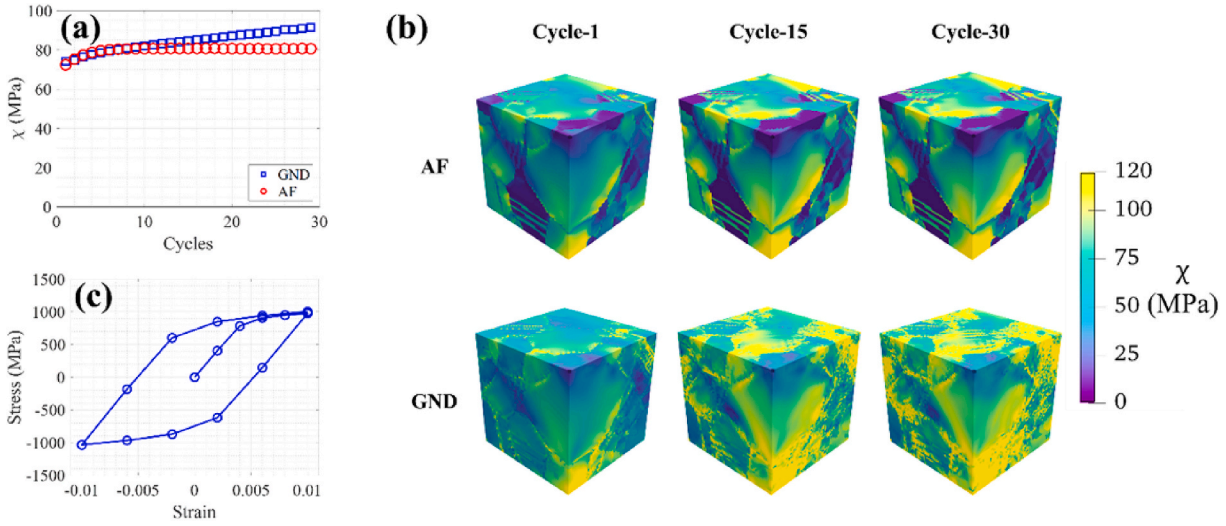

Fig. 11. (a) For $R_\varepsilon = -1$ loading, cyclic evolution of the backstress at a point within the microstructure, where the maximum value of the backstress, out of all twelve slip systems, is highest within the microstructure after the first cycle. (b) Cyclic evolution of the maximum value of backstress, out of all twelve slip systems, within the microstructure. (c) Macroscopic stress-strain response of the microstructure until one and a half cycles for the simulated loading condition in parts (a) and (b).

rapid rate, it is envisioned that constraints on computational resources would not force one to make a trade-off in the near future.

6. Conclusions

In this work, we have assessed the performance of two backstress models, namely, the empirical Armstrong-Frederick description and a GND-based backstress evolution recently proposed by Kapoor et al. (2018), in the context of crystal plasticity modeling, via comparing the simulated response of the material with the same obtained from the HEDM experiments. Key insights obtained from the present work are summarized below.

- The HEDM experiments are conducted until one and a half cycles at 1% applied strain and a strain ratio of 0. Grain-averaged stress state from the experimental data reconstruction shows strong path-dependence in the material response at the mesoscopic length-scale and provides rich information to assess the performance of the two backstress models. Both Armstrong-Frederick and GND-based models can capture the mean experimental trends quite well. However, the GND-based model better captures the grain-level heterogeneity, regarding grain size effects, especially at the macroscopic states associated with the Bauschinger effect.

- Accompanying additional simulations, carried out at 1% strain and strain ratios of 0 and -1, are conducted to 30 loading cycles and reveal that the backstress from the Armstrong-Frederick model saturates around ten cycles at both strain ratios. Further, at a strain ratio of 0, the backstress value at a significantly large number of points within the microstructure progressively approaches zero. Such predicted trends are not consistent with the experimentally observed dislocation cell structure evolution in the literature. It is these premature shakedowns or backstress relaxation behaviors that result in crystal plasticity simulations exhibiting stable hysteresis-loops and saturated micromechanical fields in only a few loading cycles, whereas these values continue to evolve in real materials. The GND-based model consistently predicts a monotonically increasing trend of backstress at both strain ratios. Such a trend is more realistic and adds more confidence to the GND-based backstress model's ability to capture the cyclic evolution of polycrystalline materials.

The present work suggests that the Armstrong-Frederick model may not be well-suited in crystal plasticity analysis, especially in the microstructure-sensitive location-specific quantitative performance analysis, such as fatigue life prediction. On the other hand, the GND-based model (a) is physics-based, (b) involves only one unknown fitting constant, and (c) captures the realistic cyclic evolution of the backstress. Thus, the GND-based model is promising in the cyclic response analysis of metals using a crystal plasticity approach.

CRediT authorship contribution statement

Ritwik Bandyopadhyay: Conceptualization, Formal analysis, Visualization, Writing - original draft. **Sven E. Gustafson:** Methodology, Validation, Investigation, Visualization, Writing - review & editing. **Kartik Kapoor:** Methodology, Software, Writing - review & editing. **Diwakar Naragani:** Investigation, Writing - review & editing. **Darren C. Pagan:** Investigation, Writing - review & editing. **Michael D. Sangid:** Conceptualization, Investigation, Funding acquisition, Supervision, Project administration, Data curation, Writing - review & editing.

Declaration of competing interest

The authors declare that they have no known competing financial interests or personal relationships that could have appeared to influence the work reported in this paper.

Acknowledgments

Financial support for this project was provided by the DARPA (grant number HR0011-12-C-0037) and the National Science Foundation (grant number CMMI 16–51956). DARPA funding was part of Phase III - "Integrated Computational Materials Engineering (ICME) approaches to additive manufacturing, fatigue, and modeling/characterization" of the Open Manufacturing Program entitled "Rapid Low Cost Additive Manufacturing" awarded to Honeywell International Inc. The authors would like to thank Dr. Alonso D. Peralta from Honeywell Aerospace for providing the material, Dr. Veerappan Prithivirajan from Purdue University for helping with microstructure model creation, the DARPA program managers Dr. Jan Vandenbrande and Mr. Mick Maher, and the NSF program manager, Dr. Alexis Lewis. RB would like to thank Prof. Ganesh Subbarayan from Purdue University for interesting discussions on the constitutive modeling in continuum mechanics. Experimental measurements were conducted at the Cornell High Energy Synchrotron Source (CHESS). CHESS is supported by the National Science Foundation under award DMR-1332208.

Appendix A. Supplementary data

Supplementary data to this article can be found online at https://doi.org/10.1016/j.ijplas.2020.102887.

References

Abel, A., Muir, H., 1972. The bauschinger effect and discontinuous yielding. Philos. Mag. A 26, 489–504. https://doi.org/10.1080/14786437208227444.

Acharya, A., Bassani, J.L., 2000. Lattice incompatibility and a gradient theory of crystal plasticity. J. Mech. Phys. Solid. 48, 1565–1595. https://doi.org/10.1016/S0022-5096(99)00075-7.

Allegheny Technologies Incorporated, 2013. ATI 718Plus® alloy technical data sheet. UNS N07818 [WWW Document]. URL https://www.atimetals.com/Products/Documents/datasheets/nickel-cobalt/nickel-based/ati_718plus_tds_en_v3.pdf. .

Anand, L., Kothari, M., 1996. A computational procedure for rate-independent crystal plasticity. J. Mech. Phys. Solid. 44, 525–558. https://doi.org/10.1016/0022-5096(96)00001-4.

Armstrong, P.J., Frederick, C.O., 1966. A Mathematical Representation of the Multiaxial Bauschinger Effect. CEGB Report, Berkeley Nuclear Laboratories. RD/B/N731.

Arsenlis, A., Parks, D.M., 1999. Crystallographic aspects of geometrically-necessary and statistically-stored dislocation density. Acta Mater. 47, 1597–1611. https://doi.org/10.1016/S1359-6454(99)00020-8.

Asaro, R.J., Needleman, A., 1985. Overview no. 42 Texture development and strain hardening in rate dependent polycrystals. Acta Metall. 33, 923–953. https://doi.org/10.1016/0001-6160(85)90188-9.

Ashby, M.F., 1970. The deformation of plastically non-homogeneous materials. Philos. Mag. A 21, 399–424. https://doi.org/10.1080/14786437008238426.

Bandyopadhyay, R., Prithivirajan, V., Peralta, A.D., Sangid, M.D., 2020. Microstructure sensitive critical plastic strain energy density criterion for fatigue life prediction across various loading regimes. Proc. R. Soc. A 476, 20190766. https://doi.org/10.1098/rspa.2019.0766.

Bandyopadhyay, R., Prithivirajan, V., Sangid, M.D., 2019. Uncertainty quantification in the mechanical response of crystal plasticity simulations. J. Occup. Med. 71, 2612–2624. https://doi.org/10.1007/s11837-019-03551-3.
Bandyopadhyay, R., Sangid, M.D., 2019. Crystal plasticity assessment of inclusion- and matrix-driven competing failure modes in a nickel-base superalloy. Acta Mater. 177, 20–34. https://doi.org/10.1016/j.actamat.2019.07.024.
Bayley, C.J., Brekelmans, W.A.M., Geers, M.G.D., 2006. A comparison of dislocation induced back stress formulations in strain gradient crystal plasticity. Int. J. Solid Struct. 43, 7268–7286. https://doi.org/10.1016/j.ijsolstr.2006.05.011.
Bennett, V.P., McDowell, D.L., 2003. Polycrystal orientation distribution effects on microslip in high cycle fatigue. Int. J. Fatig. 25, 27–39. https://doi.org/10.1016/S0142-1123(02)00057-9.
Bernier, J.V., Barton, N.R., Lienert, U., Miller, M.P., 2011. Far-field high-energy diffraction microscopy: a tool for intergranular orientation and strain analysis. J. Strain Anal. Eng. Des. 46, 527–547. https://doi.org/10.1177/0309324711405761.
Bhattacharyya, J.J., Bittmann, B., Agnew, S.R., 2019. The effect of precipitate-induced backstresses on plastic anisotropy: demonstrated by modeling the behavior of aluminum alloy, 7085. Int. J. Plast. 117, 3–20. https://doi.org/10.1016/j.ijplas.2018.04.011.
Bishop, J., Hill, R., 1951. A theory of the plastic distortion of a polycrystalline aggregate under combined stresses. Philos. Mag. A 42. https://doi.org/10.1080/14786445108561065.
Castelluccio, G.M., McDowell, D.L., 2017. Mesoscale cyclic crystal plasticity with dislocation substructures. Int. J. Plast. 98, 1–26. https://doi.org/10.1016/j.ijplas.2017.06.002.
Castelluccio, G.M., McDowell, D.L., 2015. Microstructure and mesh sensitivities of mesoscale surrogate driving force measures for transgranular fatigue cracks in polycrystals. Mater. Sci. Eng., A 639, 626–639. https://doi.org/10.1016/J.MSEA.2015.05.048.
Castelluccio, G.M., McDowell, D.L., 2014. Mesoscale modeling of microstructurally small fatigue cracks in metallic polycrystals. Mater. Sci. Eng., A 598, 34–55. https://doi.org/10.1016/j.msea.2014.01.015.
Chaboche, J.L., 1991. On some modifications of kinematic hardening to improve the description of ratchetting effects. Int. J. Plast. 7, 661–678. https://doi.org/10.1016/0749-6419(91)90050-9.
Chaboche, J.L., 1989a. Constitutive equations for cyclic plasticity. Int. J. Plast. 5, 247–302. https://doi.org/10.1016/0749-6419(89)90015-6.
Chaboche, J.L., 1989b. Constitutive equations for cyclic plasticity and cyclic viscoplasticity. Int. J. Plast. 5, 247–302. https://doi.org/10.1016/S0749-6419(96)00037-X.
Chaboche, J.L., Nouailhas, D., 1989a. Constitutive modeling of ratchetting effects-part I: experimental facts and properties of the classical models. J. Eng. Mater. Technol. Trans. ASME 111, 384–392. https://doi.org/10.1115/1.3226484.
Chaboche, J.L., Nouailhas, D., 1989b. Constitutive modeling of ratchetting effects-part II: possibilities of some additional kinematic rules. J. Eng. Mater. Technol. Trans. ASME 111, 409–416. https://doi.org/10.1115/1.3226488.
Chaboche, J.L., Van, K.D., Cordier, G., 1979. Modelization of the Strain Memory Effect on the Cyclic Hardening of 316 Stainless Steel.
Chan, L.H., 2010. Synthetic Three-Dimensional Voxel-Based Microstructures that Contain Annealing Twins. Carnegie Mellon University.
Chen, W., Voisin, T., Zhang, Y., Florien, J.B., Spadaccini, C.M., McDowell, D.L., Zhu, T., Wang, Y.M., 2019. Microscale residual stresses in additively manufactured stainless steel. Nat. Commun. 10, 1–12. https://doi.org/10.1038/s41467-019-12265-8.
Clayton, J.D., Hartley, C.S., McDowell, D.L., 2014. The missing term in the decomposition of finite deformation. Int. J. Plast. 52, 51–76. https://doi.org/10.1016/j.ijplas.2013.04.009.
Clayton, J.D., McDowell, D.L., 2003. A multiscale multiplicative decomposition for elastoplasticity of polycrystals. Int. J. Plast. 19, 1401–1444. https://doi.org/10.1016/S0749-6419(02)00109-2.
Cruzado, A., LLorca, J., Segurado, J., 2017. Modeling cyclic deformation of inconel 718 superalloy by means of crystal plasticity and computational homogenization. Int. J. Solid Struct. 122–123, 148–161. https://doi.org/10.1016/j.ijsolstr.2017.06.014.
Cruzado, A., Lucarini, S., LLorca, J., Segurado, J., 2018. Microstructure-based fatigue life model of metallic alloys with bilinear Coffin-Manson behavior. Int. J. Fatig. 107, 40–48. https://doi.org/10.1016/j.ijfatigue.2017.10.014.
Dunne, F.P.E., Kiwanuka, R., Wilkinson, A.J., 2012. Crystal plasticity analysis of micro-deformation, lattice rotation and geometrically necessary dislocation density. Proc. R. Soc. A Math. Phys. Eng. Sci. 468, 2509–2531. https://doi.org/10.1098/rspa.2012.0050.
Eghtesad, A., Knezevic, M., 2019. High-performance full-field crystal plasticity with dislocation-based hardening and slip system back-stress laws: application to modeling deformation of dual-phase steels. J. Mech. Phys. Solid. 103750. https://doi.org/10.1016/j.jmps.2019.103750.
El-Naaman, S.A., Nielsen, K.L., Niordson, C.F., 2019. An investigation of back stress formulations under cyclic loading. Mech. Mater. 130, 76–87. https://doi.org/10.1016/J.MECHMAT.2019.01.005.
Evers, L.P., Brekelmans, W.A.M., Geers, M.G.D., 2004a. Scale dependent crystal plasticity framework with dislocation density and grain boundary effects. Int. J. Solid Struct. 41, 5209–5230. https://doi.org/10.1016/j.ijsolstr.2004.04.021.
Evers, L.P., Brekelmans, W.A.M., Geers, M.G.D., 2004b. Non-local crystal plasticity model with intrinsic SSD and GND effects. J. Mech. Phys. Solid. 52, 2379–2401. https://doi.org/10.1016/j.jmps.2004.03.007.
Farooq, H., Cailletaud, G., Forest, S., Ryckelynck, D., 2020. Crystal plasticity modeling of the cyclic behavior of polycrystalline aggregates under non-symmetric uniaxial loading: global and local analyses. Int. J. Plast. 126, 102619. https://doi.org/10.1016/j.ijplas.2019.10.007.
Forest, S., 2008. Some links between Cosserat, strain gradient crystal plasticity and the statistical theory of dislocations. Philos. Mag. A 88, 3549–3563. https://doi.org/10.1080/14786430802154815.
Geers, M.G.D., Brekelmans, W.A.M., Bayley, C.J., 2007. Second-order crystal plasticity: internal stress effects and cyclic loading. Modelling and Simulation in Materials Science and Engineering. https://doi.org/10.1088/0965-0393/15/1/S12.
Goh, C.H., McDowell, D.L., Neu, R.W., 2006. Plasticity in polycrystalline fretting fatigue contacts. J. Mech. Phys. Solid. 54, 340–367. https://doi.org/10.1016/j.jmps.2005.06.009.
Goh, C.H., Neu, R.W., McDowell, D.L., 2003. Crystallographic plasticity in fretting of Ti-6AL-4V. Int. J. Plast. 19, 1627–1650. https://doi.org/10.1016/S0749-6419(02)00039-6.
Goh, C.H., Wallace, J.M., Neu, R.W., McDowell, D.L., 2001. Polycrystal plasticity simulations of fretting fatigue. Int. J. Fatig. 23, 423–435. https://doi.org/10.1016/S0142-1123(01)00150-5.
Gong, J., Deutchman, H.Z., Peralta, A., Snyder, D., Enright, M.P., Mcfarland, J., Neumann, J., Sebastian, J., Olson, G., 2016. Integrated thermal process optimization of alloy 718Plus ® for additive manufacturing. Superalloys 1031–1040. https://doi.org/10.1002/9781119075646.ch109, 2016.
Groeber, M.A., Jackson, M.A., 2014. DREAM.3D: a digital representation environment for the analysis of microstructure in 3D. Integr. Mater. Manuf. Innov. 3, 1–17. https://doi.org/10.1186/2193-9772-3-5.
Harder, J., 1999. Crystallographic model for the study of local deformation processes in polycrystals. Int. J. Plast. 15, 605–624. https://doi.org/10.1016/S0749-6419(99)00002-9.
Hasija, V., Ghosh, S., Mills, M.J., Joseph, D.S., 2003. Deformation and creep modeling in polycrystalline Ti-6Al alloys. Acta Mater. 51, 4533–4549. https://doi.org/10.1016/S1359-6454(03)00289-1.
Hennessey, C., Castelluccio, G.M., McDowell, D.L., 2017. Sensitivity of polycrystal plasticity to slip system kinematic hardening laws for Al 7075-T6. Mater. Sci. Eng., A 687, 241–248. https://doi.org/10.1016/j.msea.2017.01.070.
Hill, R., 1967. The essential structure of constitutive laws for metal composites and polycrystals. J. Mech. Phys. Solid. 15, 79–95. https://doi.org/10.1016/0022-5096(67)90018-X.
Holt, D.L., 1970. Dislocation cell formation in metals. J. Appl. Phys. 41, 3197–3201. https://doi.org/10.1063/1.1659399.
Horstemeyer, M.F., McDowell, D.L., McGinty, R.D., 1999. Design of experiments for constitutive model selection: application to polycrystal elastoviscoplasticity. Model. Simulat. Mater. Sci. Eng. 7, 253–273.

Huang, E.W., Barabash, R.I., Wang, Y., Clausen, B., Li, L., Liaw, P.K., Ice, G.E., Ren, Y., Choo, H., Pike, L.M., Klarstrom, D.L., 2008. Plastic behavior of a nickel-based alloy under monotonic-tension and low-cycle-fatigue loading. Int. J. Plast. 24, 1440–1456. https://doi.org/10.1016/j.ijplas.2007.10.001.
Hurley, R.C., Herbold, E.B., Pagan, D.C., 2018. Characterization of the crystal structure, Kinematics, stresses and rotations in angular granular quartz during compaction. J. Appl. Crystallogr. 51, 1021–1034. https://doi.org/10.1107/S1600576718006957.
Hutchinson, J.W., 1976. Bounds and self-consistent estimates for creep of polycrystalline materials. Proc. R. Soc. A Math. Phys. Eng. Sci. 348, 101–127. https://doi.org/10.1098/rspa.1976.0027.
Juul, N.Y., Winther, G., Dale, D., Koker, M.K.A., Shade, P., Oddershede, J., 2016. Elastic interaction between twins during tensile deformation of austenitic stainless steel. Scripta Mater. 120, 1–4. https://doi.org/10.1016/j.scriptamat.2016.03.022.
Kapoor, K., Sangid, M.D., 2018. Initializing type-2 residual stresses in crystal plasticity finite element simulations utilizing high-energy diffraction microscopy data. Mater. Sci. Eng., A 729, 53–63. https://doi.org/10.1016/j.msea.2018.05.031.
Kapoor, K., Yoo, Y.S.J., Book, T.A., Kacher, J.P., Sangid, M.D., 2018. Incorporating grain-level residual stresses and validating a crystal plasticity model of a two-phase Ti-6Al-4 V alloy produced via additive manufacturing. J. Mech. Phys. Solid. 121, 447–462. https://doi.org/10.1016/j.jmps.2018.07.025.
Kim, J.H., Kim, D., Barlat, F., Lee, M.G., 2012. Crystal plasticity approach for predicting the Bauschinger effect in dual-phase steels. Mater. Sci. Eng., A 539, 259–270. https://doi.org/10.1016/j.msea.2012.01.092.
Kocks, U.F., 1970. The relation between polycrystal deformation and single-crystal deformation. Metall. Mater. Trans. B 1, 1121–1143. https://doi.org/10.1007/BF02900224.
Kuhlmann-Wilsdorf, D., 1989. Theory of plastic deformation: - properties of low energy dislocation structures. Mater. Sci. Eng., A 113, 1–41. https://doi.org/10.1016/0921-5093(89)90290-6.
Kuhlmann-Wilsdorf, D., Laird, C., 1977. Dislocation behavior in fatigue. Mater. Sci. Eng. 27, 137–156. https://doi.org/10.1016/0025-5416(77)90166-5.
Kuhlmann-Wilsdorf, D., Van Der Merwe, J.H., 1982. Theory of dislocation cell sizes in deformed metals. Mater. Sci. Eng. 55, 79–83. https://doi.org/10.1016/0025-5416(82)90086-6.
Laufer, E.E., Roberts, W.N., 1964. Dislocation structures in fatigued copper single crystals. Philos. Mag. A 10, 883–885. https://doi.org/10.1080/14786436408225391.
Lee, E.H., 1969. Elastic-plastic deformation at finite strains. J. Appl. Mech. 36, 1–6. https://doi.org/10.1115/1.3564580.
Li, L., Shen, L., Proust, G., 2014. A texture-based representative volume element crystal plasticity model for predicting Bauschinger effect during cyclic loading. Mater. Sci. Eng., A 608, 174–183. https://doi.org/10.1016/j.msea.2014.04.067.
Li, S.F., Suter, R.M., 2013. Adaptive reconstruction method for three-dimensional orientation imaging. J. Appl. Crystallogr. 46, 512–524. https://doi.org/10.1107/S0021889813005268.
Margulies, L., Lorentzen, T., Poulsen, H.F., Leffers, T., 2002. Strain tensor development in a single grain in the bulk of a polycrystal under loading. Acta Mater. 50, 1771–1779. https://doi.org/10.1016/S1359-6454(02)00028-9.
Mayeur, J.R., McDowell, D.L., 2015. Micropolar crystal plasticity simulation of particle strengthening. Model. Simulat. Mater. Sci. Eng. 23, 065007 https://doi.org/10.1088/0965-0393/23/6/065007.
Mayeur, J.R., McDowell, D.L., 2014. A comparison of Gurtin type and micropolar theories of generalized single crystal plasticity. Int. J. Plast. 57, 29–51. https://doi.org/10.1016/j.ijplas.2014.01.010.
Mayeur, J.R., McDowell, D.L., 2013. An evaluation of higher-order single crystal strength models for constrained thin films subjected to simple shear. J. Mech. Phys. Solid. 61, 1935–1954. https://doi.org/10.1016/j.jmps.2013.04.007.
Mayeur, J.R., McDowell, D.L., 2007. A three-dimensional crystal plasticity model for duplex Ti-6Al-4V. Int. J. Plast. 23, 1457–1485. https://doi.org/10.1016/j.ijplas.2006.11.006.
Mayeur, J.R., McDowell, D.L., Bammann, D.J., 2011. Dislocation-based micropolar single crystal plasticity: comparison of multi- and single criterion theories. J. Mech. Phys. Solid. 59, 398–422. https://doi.org/10.1016/j.jmps.2010.09.013.
Mayeur, J.R., McDowell, D.L., Neu, R.W., 2008. Crystal plasticity simulations of fretting of Ti-6Al-4V in partial slip regime considering effects of texture. Comput. Mater. Sci. 41, 356–365. https://doi.org/10.1016/j.commatsci.2007.04.020.
McDowell, D.L., 1995. Stress state dependence of cyclic ratchetting behavior of two rail steels. Int. J. Plast. https://doi.org/10.1016/S0749-6419(95)00005-4.
McDowell, D.L., Moosbrugger, J.C., 1990. Application of Continuum Slip Approaches to Viscoplasticity. Springer, Dordrecht, pp. 295–303. https://doi.org/10.1007/978-94-009-1968-6_34.
McGinty, R.D., 2001. Multiscale Representation of Polycrystalline Inelasticity. Georgia Institute of Technology.
Méric, L., Cailletaud, G., 1991. Single crystal modeling for structural calculations: Part 2-finite element implementation. J. Eng. Mater. Technol. Trans. ASME 113, 171–182. https://doi.org/10.1115/1.2903375.
Méric, L., Poubanne, P., Cailletaud, G., 1991. Single crystal modeling for structural calculations: Part 1-model presentation. J. Eng. Mater. Technol. Trans. ASME 113, 162–170. https://doi.org/10.1115/1.2903374.
Miller, M.P., McDowell, D.L., 1996. Modeling large strain multiaxial effects in FCC polycrystals. Int. J. Plast. 12, 875–902. https://doi.org/10.1016/S0749-6419(96)00032-0.
Mughrabi, H., 2006. Deformation-induced long-range internal stresses and lattice plane misorientations and the role of geometrically necessary dislocations. Philos. Mag. A 86, 4037–4054. https://doi.org/10.1080/14786430500509054.
Mughrabi, H., 1983. Dislocation wall and cell structures and long-range internal stresses in deformed metal crystals. Acta Metall. 31, 1367–1379.
Mughrabi, H., Ungár, T., 2006. Close up on crystal plasticity. Nat. Mater. 5, 601–602. https://doi.org/10.1038/nmat1706.
Muhammad, W., Brahme, A.P., Kang, J., Mishra, R.K., Inal, K., 2017. Experimental and numerical investigation of texture evolution and the effects of intragranular backstresses in aluminum alloys subjected to large strain cyclic deformation. Int. J. Plast. 93, 137–163. https://doi.org/10.1016/j.ijplas.2016.11.003.
Naragani, D.P., Shade, P.A., Kenesei, P., Sharma, H., Sangid, M.D., 2019. X-ray characterization of the micromechanical response ahead of a propagating small fatigue crack in a Ni-based superalloy. Acta Mater. 179, 342–359. https://doi.org/10.1016/j.actamat.2019.08.005.
Neumann, P., 1986. Low energy dislocation configurations: a possible key to the understanding of fatigue. Mater. Sci. Eng. 81, 465–475. https://doi.org/10.1016/0025-5416(86)90284-3.
Nye, J.F., 1953. Some geometrical relations in dislocated crystals. Acta Metall. 1, 153–162. https://doi.org/10.1016/0001-6160(53)90054-6.
Obstalecki, M., Wong, S.L., Dawson, P.R., Miller, M.P., 2014. Quantitative analysis of crystal scale deformation heterogeneity during cyclic plasticity using high-energy X-ray diffraction and finite-element simulation. Acta Mater. 75, 259–272. https://doi.org/10.1016/j.actamat.2014.04.059.
Oddershede, J., Schmidt, Sø, Poulsen, H.F., Srensen, H.O., Wright, J., Reimers, W., 2010. Determining grain resolved stresses in polycrystalline materials using three-dimensional X-ray diffraction. J. Appl. Crystallogr. 43, 539–549. https://doi.org/10.1107/S0021889810012963.
Ohno, N., Wang, J.D., 1993a. Kinematic hardening rules with critical state of dynamic recovery, part II: application to experiments of ratchetting behavior. Int. J. Plast. 9, 391–403. https://doi.org/10.1016/0749-6419(93)90043-.
Ohno, N., Wang, J.D., 1993b. Kinematic hardening rules with critical state of dynamic recovery, part I: formulation and basic features for ratchetting behavior. Int. J. Plast. 9, 375–390. https://doi.org/10.1016/0749-6419(93)90042-O.
Pagan, D.C., Bernier, J.V., Dale, D., Ko, J.Y.P., Turner, T.J., Blank, B., Shade, P.A., 2018. Measuring Ti-7Al slip system strengths at elevated temperature using high-energy X-ray diffraction. Scripta Mater. 142, 96–100. https://doi.org/10.1016/j.scriptamat.2017.08.029.
Pagan, D.C., Miller, M.P., 2014. Connecting heterogeneous single slip to diffraction peak evolution in high-energy monochromatic X-ray experiments. J. Appl. Crystallogr. 47, 887–898. https://doi.org/10.1107/S1600576714005779.
Peralta, A.D., Enright, M., Megahed, M., Gong, J., Roybal, M., Craig, J., 2016. Towards rapid qualification of powder-bed laser additively manufactured parts. Integr. Mater. Manuf. Innov. 5, 8. https://doi.org/10.1186/s40192-016-0052-5.
Poulsen, H., 2004. Three-Dimensional X-Ray Diffraction Microscopy, Springer Tracts in Modern Physics. Springer Berlin Heidelberg, Berlin, Heidelberg. https://doi.org/10.1007/b97884.

Prasannavenkatesan, R., McDowell, D.L., 2010. Polycrystal plasticity modeling of cyclic residual stress relaxation in shot peened martensitic gear steel. J. Eng. Mater. Technol. Trans. ASME 132. https://doi.org/10.1115/1.4001594, 0310111–0310118.
Prithivirajan, V., Sangid, M.D., 2020. Examining metrics for fatigue life predictions of additively manufactured IN718 via crystal plasticity modeling including the role of simulation volume and microstructural constraints. Mater. Sci. Eng., A 139312. https://doi.org/10.1016/j.msea.2020.139312.
Prithivirajan, V., Sangid, M.D., 2018. The role of defects and critical pore size analysis in the fatigue response of additively manufactured IN718 via crystal plasticity. Mater. Des. 150, 139–153. https://doi.org/10.1016/j.matdes.2018.04.022.
Rice, J.R., 1971. Inelastic constitutive relations for solids: an internal-variable theory and its application to metal plasticity. J. Mech. Phys. Solid. 19, 433–455. https://doi.org/10.1016/0022-5096(71)90010-X.
Rice, J.R., 1970. On the structure of stress-strain relations for time-dependent plastic deformation in metals. J. Appl. Mech. Trans. ASME 37, 728–737. https://doi.org/10.1115/1.3408603.
Sangid, M.D., Maier, H.J., Sehitoglu, H., 2011. An energy-based microstructure model to account for fatigue scatter in polycrystals. J. Mech. Phys. Solid. 59, 595–609. https://doi.org/10.1016/j.jmps.2010.12.014.
Sangid, M.D., Yeratapally, S.R., Rovinelli, A., 2014. Validation of microstructure-based materials modeling. In: 55th AIAA/ASMe/ASCE/AHS/SC Structures, Structural Dynamics, and Materials Conference. https://doi.org/10.2514/6.2014-0462.
Sauzay, M., 2008. Analytical modelling of intragranular backstresses due to deformation induced dislocation microstructures. Int. J. Plast. 24, 727–745. https://doi.org/10.1016/j.ijplas.2007.07.004.
Schäfer, B.J., Song, X., Sonnweber-Ribic, P., Hassan, H.U., Hartmaier, A., 2019. Micromechanical modelling of the cyclic deformation behavior of martensitic sae 4150-a comparison of different kinematic hardening models. Metals 9. https://doi.org/10.3390/met9030368.
Schuren, J.C., Miller, M.P., 2011. Quantifying the uncertainty of synchrotron-based lattice strain measurements. J. Strain Anal. Eng. Des. 46, 663–681. https://doi.org/10.1177/0309324711411553.
Schuren, J.C., Shade, P.A., Bernier, J.V., Li, S.F., Blank, B., Lind, J., Kenesei, P., Lienert, U., Suter, R.M., Turner, T.J., Dimiduk, D.M., Almer, J., 2015. New opportunities for quantitative tracking of polycrystal responses in three dimensions. Curr. Opin. Solid State Mater. Sci. 19, 235–244. https://doi.org/10.1016/j.cossms.2014.11.003.
Shade, P.A., Blank, B., Schuren, J.C., Turner, T.J., Kenesei, P., Goetze, K., Suter, R.M., Bernier, J.V., Li, S.F., Lind, J., Lienert, U., Almer, J., 2015. A rotational and axial motion system load frame insert for in situ high energy x-ray studies. Rev. Sci. Instrum. 86 https://doi.org/10.1063/1.4927855.
Shade, P.A., Musinski, W.D., Obstalecki, M., Pagan, D.C., Beaudoin, A.J., Bernier, J.V., Turner, T.J., 2019. Exploring new links between crystal plasticity models and high-energy X-ray diffraction microscopy. Curr. Opin. Solid State Mater. Sci. https://doi.org/10.1016/j.cossms.2019.07.002.
Shenoy, M., Tjiptowidjojo, Y., McDowell, D., 2008. Microstructure-sensitive modeling of polycrystalline IN 100. Int. J. Plast. 24, 1694–1730. https://doi.org/10.1016/j.ijplas.2008.01.001.
Sleeswyk, A.W., James, M.R., Plantinga, D.H., Maathuis, W.S.T., 1978. Reversible strain in cyclic plastic deformation. Acta Metall. 26, 1265–1271.
Smith, B.D., Shih, D.S., McDowell, D.L., 2018. Cyclic plasticity experiments and polycrystal plasticity modeling of three distinct Ti alloy microstructures. Int. J. Plast. 101, 1–23. https://doi.org/10.1016/j.ijplas.2013.10.004.
Suresh, S., 1998. Fatigue of Materials. Cambridge University Press. https://doi.org/10.5860/choice.29-4547.
Suter, R.M., Hennessy, D., Xiao, C., Lienert, U., 2006. Forward modeling method for microstructure reconstruction using x-ray diffraction microscopy: single-crystal verification. Rev. Sci. Instrum. 77 https://doi.org/10.1063/1.2400017.
Taylor, G.I., 1934. The mechanism of plastic deformation of crystals. Part I. Theoretical. Proc. R. Soc. A Math. Phys. Eng. Sci. 145, 362–387. https://doi.org/10.1098/rspa.1934.0106.
Tu, X., Shahba, A., Shen, J., Ghosh, S., 2019. Microstructure and property based statistically equivalent RVEs for polycrystalline-polyphase aluminum alloys. Int. J. Plast. 115, 268–292. https://doi.org/10.1016/j.ijplas.2018.12.002.
Ungar, T., Mughrabi, H., Rönnpagel, D., Wilkens, M., 1984. X-ray line-broadening study of the dislocation cell structure in deformed [001]-orientated copper single crystals. Acta Metall. 32, 333–342. https://doi.org/10.1016/0001-6160(84)90106-8.
Venkataramani, G., Deka, D., Ghosh, S., Nordholt, J.B., 2006. Crystal plasticity based Fe model for understanding microstructural effects on creep and dwell fatigue in Ti-6242. J. Eng. Mater. Technol. Trans. ASME 128, 356–365. https://doi.org/10.1115/1.2204942.
Venkataramani, G., Kirane, K., Ghosh, S., 2008. Microstructural parameters affecting creep induced load shedding in Ti-6242 by a size dependent crystal plasticity FE model. Int. J. Plast. 24, 428–454. https://doi.org/10.1016/j.ijplas.2007.05.001.
Wang, R., Mughrabi, H., 1984. Secondary cyclic hardening in fatigued copper monocrystals and polycrystals. Mater. Sci. Eng. 63, 147–163. https://doi.org/10.1016/0025-5416(84)90118-6.
Wang, R., Mughrabi, H., McGovern, S., Rapp, M., 1984. Fatigue of copper single crystals in vacuum and in air I: persistent slip bands and dislocation microstructures. Mater. Sci. Eng. 65, 219–233. https://doi.org/10.1016/0025-5416(84)90084-3.
Wollmershauser, J.A., Clausen, B., Agnew, S.R., 2012. A slip system-based kinematic hardening model application to in situ neutron diffraction of cyclic deformation of austenitic stainless steel. Int. J. Fatig. 36, 181–193. https://doi.org/10.1016/j.ijfatigue.2011.07.008.
Woods, P.J., 1973. Low-amplitude fatigue of copper and copper-5 at. % aluminium single crystals. Philos. Mag. A 28, 155–191. https://doi.org/10.1080/14786437308217440.
Xie, C.L., Ghosh, S., Groeber, M., 2004. Modeling cyclic deformation of HSLA steels using crystal plasticity. J. Eng. Mater. Technol. Trans. ASME 126, 339–352. https://doi.org/10.1115/1.1789966.
Zecevic, M., Knezevic, M., 2015. A dislocation density based elasto-plastic self-consistent model for the prediction of cyclic deformation: application to AA6022-T4. Int. J. Plast. 72, 200–217. https://doi.org/10.1016/j.ijplas.2015.05.018.
Zhang, M., Bridier, F., Villechaise, P., Mendez, J., McDowell, D.L., 2010. Simulation of slip band evolution in duplex Ti-6Al-4V. Acta Mater. 58, 1087–1096. https://doi.org/10.1016/j.actamat.2009.10.025.
Zhang, M., Zhang, J., McDowell, D.L., 2007. Microstructure-based crystal plasticity modeling of cyclic deformation of Ti-6Al-4V. Int. J. Plast. 23, 1328–1348. https://doi.org/10.1016/j.ijplas.2006.11.009.
Zheng, Z., Prastiti, N.G., Balint, D.S., Dunne, F.P.E., 2019. The dislocation configurational energy density in discrete dislocation plasticity. J. Mech. Phys. Solid. 129, 39–60. https://doi.org/10.1016/J.JMPS.2019.04.015.